

Morphology of Galaxies in JWST Fields: Initial Distribution and Evolution of Galaxy Morphology

JEONG HWAN LEE,^{1,2} CHANGBOM PARK,³ HO SEONG HWANG,^{4,5} AND MINSEONG KWON⁴

¹*Department of Astronomy and Atmospheric Sciences, Kyungpook National University, Daegu 41566, Republic of Korea*

²*The Center for High Energy Physics, Kyungpook National University, Daegu 41566, Republic of Korea*

³*Korea Institute for Advanced Study, 85 Hoegi-ro, Dongdaemun-gu, Seoul 02455, Republic of Korea*

⁴*Department of Physics and Astronomy, Seoul National University, 1 Gwanak-ro, Gwanak-gu, Seoul 08826, Republic of Korea*

⁵*SNU Astronomy Research Center, Seoul National University, 1 Gwanak-ro, Gwanak-gu, Seoul 08826, Republic of Korea*

ABSTRACT

A recent study from the Horizon Run (HR5) cosmological simulation has predicted that galaxies with $\log M_*/M_\odot \lesssim 10$ in the cosmic morning ($10 \gtrsim z \gtrsim 4$) dominantly have disk-like morphology in the Λ CDM universe, which is driven by the tidal torque in the initial matter fluctuations. For a direct comparison with observation, we identify a total of about 19,000 James Webb Space Telescope (JWST) galaxies with $\log M_*/M_\odot > 9$ at $z = 0.6\text{--}8.0$ utilizing deep JWST/NIRCam images of publicly released fields, including NEP-TDF, NGDEEP, CEERS, COSMOS, UDS, and SMACS J0723–7327. We estimate their stellar masses and photometric redshifts with the redshift dispersion of $\sigma_{\text{NMAD}} = 0.009$ and outlier fraction of only about 6%. We classify galaxies into three morphological types, ‘disks’, ‘spheroids’, and ‘irregulars’, applying the same criteria used in the HR5 study. The morphological distribution of the JWST galaxies shows that disk galaxies account for 60–70% at all redshift ranges. However, in the high-mass regime ($\log M_*/M_\odot \gtrsim 11$), spheroidal morphology becomes the dominant type. This implies that mass growth of galaxies is accompanied with morphological transition from disks to spheroids. The fraction of irregulars is about 20% or less at all mass and redshifts. All the trends in the morphology distribution are consistently found in the six JWST fields. These results are in close agreement with the results from the HR5 simulation, particularly confirming the prevalence of disk galaxies at small masses in the cosmic morning and noon.

1. INTRODUCTION

Since the Hubble’s tuning fork scheme for galaxy classification was introduced (Hubble 1926; Sandage 1961), galaxy morphology has provided important insights into the evolution of galaxies across cosmic time. Previous studies have found that galaxy morphology is closely involved with the environment and various intrinsic properties of galaxies such as luminosity, mass, and star formation activity. For instance, the morphology-density and morphology-radius relations (Dressler 1980; Postman et al. 2005; Park et al. 2007; Park & Hwang 2009; Fasano et al. 2015) demonstrated that the proportion of early-type galaxies (ellipticals and S0 galaxies) in galaxy clusters increases as clustercentric distance decreases and galaxy number density increases. These re-

lationships are also dependent on the stellar mass of galaxies, showing significantly high fractions of early-type galaxies ($\gtrsim 50\%$) for galaxies more massive than $\log M_*/M_\odot > 11$ (morphology-mass relation; Bamford et al. 2009; Vulcani et al. 2011; Calvi et al. 2012). Furthermore, several studies using the Sloan Digital Sky Survey (SDSS) data suggested that the morphology of neighboring galaxies also plays an important role in the morphological distribution of galaxies in local universe (Park et al. 2008; Park & Choi 2009) and in the Great Observatories Origins Deep Survey (GOODS) field at up to $z \sim 1$ (Hwang & Park 2009). They showed that the early-type probability of a galaxy increases when the galaxy is closer to another early-type neighbor galaxy, whereas the probability decreases when the neighbor is a late-type galaxy. In addition, Hwang & Park (2009) showed that the morphology-density relation becomes much weaker at $z \sim 1$ compared to the nearby universe, implying that the morphological distribution of galaxies must depend on redshift.

Beyond $z > 1$, high-resolution optical and near-infrared (NIR) images from the Hubble Space Telescope (HST) have been used for investigating the morphology of galaxies. Most studies utilizing HST data have consistently reported that galaxies at $z \sim 2$ exhibit a high prevalence of disturbed or interacting morphologies, which are categorized as peculiar types (Abraham & van den Bergh 2001; Conselice et al. 2005, 2008; Papovich et al. 2005; Huertas-Company et al. 2009, 2016; Buitrago et al. 2013; Mortlock et al. 2013).

However, there have been two major problems in previous HST studies on high-redshift galaxy morphology. First, there are notable discrepancies in the specific trends of morphological distributions. Buitrago et al. (2013) presented that the fraction of disk-like galaxies increases from approximately 15% at $z \sim 0$ to $\sim 80\%$ at $z > 2$, whereas the fraction of spheroid-like galaxies decreases from $\sim 85\%$ to $\sim 20\%$ over the same redshift range, based on the data from the Palomar Observatory Wide-field InfraRed/DEEP2 (POWIR/DEEP2) and GOODS NICMOS Survey (GNS) surveys. In contrast, Mortlock et al. (2013) found a high fraction of spheroidal galaxies (40%) and a negligible number of disk-like galaxies ($< 10\%$) at $z > 2$ in the Ultra Deep Survey (UDS) region of the Cosmic Assembly Near-infrared Deep Extragalactic Legacy Survey (CANDELS) field. These discrepancies could be attributed to variations in the criteria for morphological classification and sample selection. For instance, Buitrago et al. (2013) selected massive galaxies ($\log M_*/M_\odot > 11$) and classified their morphologies mainly based on their Sérsic indices, while Mortlock et al. (2013) only visually classified the morphology of galaxies with $\log M_*/M_\odot > 10$. Second, HST optical and NIR data have observational limitations for studying high-redshift galaxy morphology at $z \gtrsim 3$. The longest wavelength coverage of the HST extends to $\sim 1.6\mu\text{m}$ (WFC3-IR/F160W), restricting investigations of galaxy morphology to $z \lesssim 2.5$ in the rest-frame optical wavelength range. Furthermore, the spatial resolution of NIR (WFC3-IR) data is worse than that of HST optical (ACS) data, showing a full width at half maximum (FWHM) twice as broad ($\sim 0''.2$) as that from the HST/ACS images. These limitations pose challenges when studying the morphology of high-redshift galaxies.

Thanks to the unprecedented sensitivity and resolution of the James Webb Space Telescope (JWST), there have been dramatic advances in observational studies of high-redshift galaxy morphology. Recent JWST studies have utilized various methods for classifying galaxy morphology, including visual inspections (Ferreira et al. 2022, 2023; Jacobs et al. 2023; Kar-

taltepe et al. 2023), supervised Convolutional Neural Networks (Huertas-Company et al. 2023), the Morphheus deep-learning framework (Robertson et al. 2023), and unsupervised machine learning (Tohill et al. 2023; Vega-Ferrero et al. 2024). Ferreira et al. (2022, 2023) conducted visual classifications of galaxy morphology combined with nonparametric measurements of concentration, asymmetry, and smoothness (CAS; Conselice 2003), using JWST/NIRCam images of the SMACS 0723 and the Cosmic Evolution Early Release Science Survey (CEERS) fields. They concluded that disk galaxies are predominant at $z = 3 - 6$, constituting $> 40\%$ of galaxies with $\log M_*/M_\odot > 9$. With a sample of 850 galaxies from the CEERS field, Kartaltepe et al. (2023) also found a high fraction of disk galaxies, comprising 60% at $z \sim 3$ and 30% at $z > 6$, while the fractions of spheroid and irregular galaxies are relatively constant at all redshifts. Huertas-Company et al. (2023) and Tohill et al. (2023) investigated the morphology of a relatively larger sample of galaxies at $z > 2$ by employing artificial intelligence techniques. They demonstrated that the fractions of clumpy and irregular galaxies increase with increasing redshift, while the fractions of spheroid-like galaxies decrease. Vega-Ferrero et al. (2024) explored the morphological distribution of high-redshift galaxies at $z \sim 3 - 6$ using a contrastive learning framework. They found that the fraction of disk galaxies might be overestimated, attributed to the misclassification of compact prolate-shaped galaxies as disks. Overall, recent JWST studies are in agreement that the Hubble Sequence, encompassing diverse morphologies from disk galaxies to spheroid galaxies, was already established in the early universe at $z \sim 8 - 9$. This agreement results from the superior observational performance of the JWST, which have improved the visibility of regular morphological features such as disks, bulges, and spiral arms compared to HST (Jacobs et al. 2023).

In this work, we examine the rest-frame optical morphologies of a large sample of $\sim 19,000$ galaxies at $z = 0.6 - 8.0$ using data from six public fields of JWST. We have improved the accuracy of photometric redshifts significantly, which can potentially impact the study of redshift evolution of galaxy morphology. **Figure 1** displays the rest-frame pivot wavelengths of JWST/NIRCam filters (F115W, F150W, F200W, F277W, F356W, and F444W) as a function of redshift. To probe the galaxy morphology, we choose the NIRCam filter to observe the galaxies in rest-frame optical wavelengths ($0.5 - 0.7\mu\text{m}$) at the corresponding redshifts. We then compare these galaxy morphologies with the recent findings from Horizon Run 5 (HR5) cosmological simulation (Lee et al. 2021). The HR5 results from Park et al. (2022) sug-

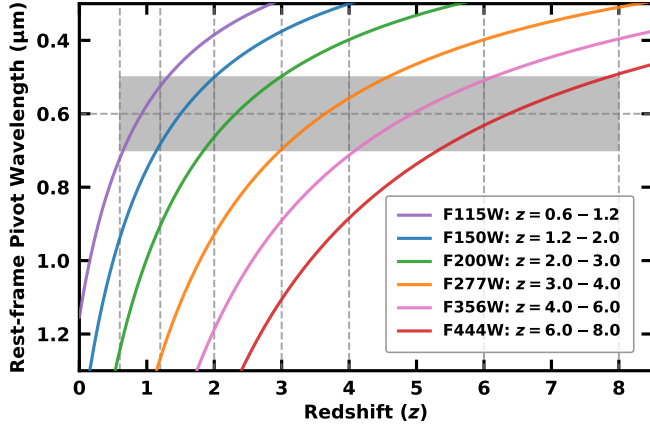


Figure 1. Rest-frame pivot wavelengths of JWST/NIRCam filters (F115W, F150W, F200W, F277W, F356W, and F444W) as a function of redshift. The shaded gray region represents the rest-frame optical wavelength range spanning $0.5 - 0.7 \mu\text{m}$.

gested that approximately two-thirds of the galaxies with $M_* \leq 10^{10} M_\odot$ in the cosmic morning ($10 \gtrsim z \gtrsim 4$) exhibit disk-like morphologies, implying the dominance of disks in the early universe. The remaining galaxies are roughly equally divided into irregulars and spheroids, with a slight prevalence of irregulars. Our objective is to verify if these HR5 results are supported by observational evidence, using high-redshift galaxies detected in JWST/NIRCam images when the morphology classification criteria as close as those used in HR5 are applied. To achieve this scientific goal, we selected galaxies with stellar mass of $M_* > 10^9 M_\odot$ across a wide range of redshifts ($z = 0.6 - 8.0$). In line with the HR5 study, we applied the same morphology classification scheme as depicted in Figure 2 of Park et al. (2022).

This paper is structured as follows. In Section 2.1, we explain the HST and JWST images used in our analysis. Sections 2.2 and 2.3 describe how we conducted multi-wavelength photometry and estimated photometric redshifts and stellar masses of galaxies through spectral energy distribution (SED) fitting. Section 3 describes the application of the galaxy classification scheme, with measurements of Sérsic indices and asymmetry. In Section 4, we illustrate our major findings about the morphological fractions as a function of redshift and stellar mass. In Section 5, we discuss the implications of our results, including a comparison with the HR5 study. Finally, Section 6 summarizes our key results. Throughout this paper, we adopt the cosmological parameters in the Planck 2015 results (Planck Collaboration et al.

2016), which are also employed in the HR5 simulation (Lee et al. 2021): $H_0 = 68.4 \text{ km s}^{-1} \text{ Mpc}^{-1}$, $\Omega_M = 0.3$, $\Omega_\Lambda = 0.7$, $\Omega_b = 0.047$, and $\sigma_8 = 0.816$.

2. DATA AND METHODS

2.1. HST and JWST/NIRCam Images

In this study, we made use of publicly available images of HST and JWST/NIRCam from the Grizli Image Release v6.0¹, which was reduced and processed by the GRIZLI pipeline (Brammer 2023a). This pipeline has been known to be effective to alleviate instrumental artifacts in JWST countrate products (`*rate.fits`), including vertical and horizontal stripes from electronic read noise (commonly known as ‘ $1/f$ noise’; Schlawin et al. 2020), circular patterns by significant cosmic ray events (‘snowballs’), and stray light features like ‘wisps’ and ‘claws’ (Rigby et al. 2023). After correcting these artifacts, the pipeline aligned the HST and JWST/NIRCam images using stars from GAIA DR3 catalog (Gaia Collaboration et al. 2021), and combined those images. Detailed information about the image reduction process was provided in previous JWST studies (Bezanson et al. 2022; Bradley et al. 2023; Valentino et al. 2023). The final mosaic images are sampled at pixel scales of $0''.04 \text{ pixel}^{-1}$ for HST and JWST/NIRCam long wavelength channels (F277W, F356W, and F444W) and $0''.02 \text{ pixel}^{-1}$ for JWST/NIRCam short wavelength channels (F090W, F115W, F150W, and F200W). For our analysis, we resampled the NIRCam short-wavelength images to $0''.04 \text{ pixel}^{-1}$ using the Python-based tool `astropy reproject`².

We obtained the processed HST and JWST images of six public fields: the North Ecliptic Pole Time-Domain Fields (NEP-TDF; Windhorst et al. 2022, 2023), the Next Generation Deep Extragalactic Exploratory Public (NGDEEP) Survey (Finkelstein et al. 2021; Bagley et al. 2023), the CEERS (Finkelstein et al. 2017, 2023), the Cosmic Evolution Survey (COSMOS; Dunlop et al. 2021; Kartaltepe et al. 2021; Casey et al. 2023), the UKIRT Infrared Deep Sky Survey Ultra-deep Survey field (UDS; Dunlop et al. 2021), and the SMACS J0723.3-7327 cluster (SMACS0723; Pontoppidan et al. 2022). Table 1 summarizes the HST and JWST images used in our spectral energy distribution (SED) analysis, excluding images from filters with either excessively narrow coverage areas (e.g., HST F105W in most fields) or

¹ <https://s3.amazonaws.com/grizli-v2/JwstMosaics/v6/index.html>
<https://grizli.readthedocs.io/en/stable/grizli/image-release-v6.html>

² <https://github.com/astropy/reproject>

Table 1. HST and JWST Images and Filters Used in This Study

Field	Telescope	Instrument	Filters	Coverage Area ^a (arcmin ²)
NEP-TDF	HST	ACS	F435W, F606W	22.0
	JWST	NIRCam (SWC)	F090W, F115W, F150W, F200W	10.5
		NIRCam (LWC)	F277W, F356W, F410M, F444W	10.0
NGDEEP	HST	ACS	F435W, F606W, F775W, F814W, F850LP	37.3
		WFC3-IR	F105W, F125W, F160W	30.7
	JWST	NIRCam (SWC)	F115W, F150W, F200W	11.2
		NIRCam (LWC)	F277W, F356W, F444W	9.4
CEERS	HST	ACS	F435W, F606W, F814W	201.3
		WFC3-IR	F125W, F140W, F160W	167.4
	JWST	NIRCam (SWC)	F115W, F150W, F200W	89.9
		NIRCam (LWC)	F277W, F356W, F410M, F444W	91.7
COSMOS	HST	ACS	F435W, F475W, F606W, F814W	245.6
		WFC3-IR	F125W, F140W, F160W	241.3
	JWST	NIRCam (SWC)	F090W, F115W, F150W, F200W	86.8
		NIRCam (LWC)	F277W, F356W, F410M, F444W	88.9
UDS	HST	ACS	F435W, F606W, F814W	202.8
		WFC3-IR	F125W, F140W, F160W	186.6
	JWST	NIRCam (SWC)	F090W, F115W, F150W, F200W	147.4
		NIRCam (LWC)	F277W, F356W, F410M, F444W	150.8
SMACS0723	HST	ACS	F606W, F814W	12.3
		WFC3-IR	F105W, F125W, F140W, F160W	5.5
	JWST	NIRCam (SWC)	F090W, F150W, F200W	11.4
		NIRCam (LWC)	F277W, F356W, F444W	11.0

Note.

^a Areas are measured based on the image observed by the instrument’s filter with the longest wavelength.

shallow depths (e.g., HST F275W in CEERS and HST F435W in SMACS0723).

Figure 2 illustrates the surface brightness limit and coverage area of each JWST field in various NIRCam filters. We measured the 1σ surface brightness levels above the background within circular apertures with a radius of $0''.5$. For these measurements, we randomly selected 100 circular apertures per field of view of $2''.2 \times 2''.2$, corresponding to a single JWST/NIRCam module. Overall, the JWST NIRCam images exhibit surface brightness limits deeper than ~ 25 mag arcsec⁻² for the short-wavelength filters and ~ 26 mag arcsec⁻² for the long-wavelength filters, which even enables the detection of low surface brightness galaxies (Ikeda et al. 2023). The NGDEEP ($\mu_{\text{lim}}(\text{F444W}) \sim 28.0$ mag arcsec⁻²) and UDS (coverage of ~ 150 arcmin²) are the deepest and widest fields in this study, respectively.

2.2. Multiwavelength Photometry

For target selection and SED analysis for high-redshift galaxies, we performed source detection and

aperture photometry on HST and JWST images using SOURCE EXTRACTOR version 2.25.0³ (SEXTRACTOR; Bertin & Arnouts 1996). We employed the combined images of the NIRCam long-wavelength filters (F277W+F356W+F444W) as the reference images for performing forced photometry on both HST and JWST images. We utilized a two-mode detection process with ‘cold’ and ‘hot’ modes as applied in Galametz et al. (2013). The cold-mode configurations were adjusted to prevent overblending of large and bright sources, whereas the hot-mode configurations were set to detect faint objects close to bright sources. **Table 2** lists the input configuration parameters for the cold-mode and hot-mode detections of SEXTRACTOR. In the case of SMACS0723 cluster, we adjusted the configuration parameters slightly to obtain sharper background estimation due to intense intracluster light. Subsequently, we combined the source catalogs from the two-mode pho-

³ <https://github.com/astromatic/sextractor>

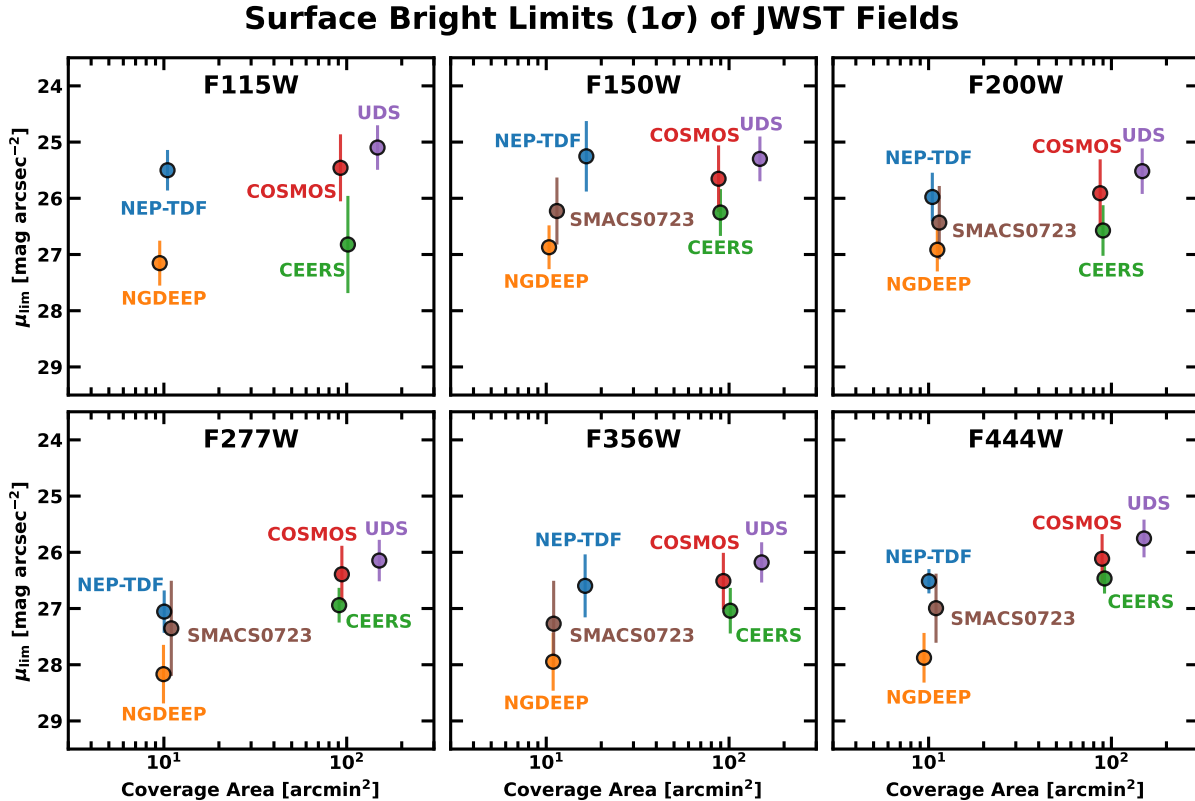


Figure 2. Distributions of surface brightness limits and coverage areas for JWST NIRCcam filters (F115W, F150W, F200W, F277W, F356W, and F444W). Surface brightness limits are measured within apertures with a radius of $0''.5$. Note that the SMACS0723 field has no JWST images from F115W.

tometry, by retaining all sources from the cold mode and supplementing them with hot-mode sources located outside the Kron radii of cold-mode sources (Barden et al. 2012; Kartaltepe et al. 2023). The merged source catalogs include various objects other than galaxies such as cosmic rays, artifacts, or foreground stars. Therefore, we initially selected galaxy candidates using specific criteria based on colors and sizes as shown in Figure 3. We applied realistic color ranges ($-1.5 < F200W - F277W < 1.5$ and $-1.5 < F277W - F356W < 1.5$) and $FLAGS \leq 4$ to remove artifacts. These color ranges were chosen to reflect the typical JWST/NIRCcam colors of stellar populations within galaxies, and the FLAGS effectively filtered out saturated sources or those close to image edges. Furthermore, to minimize contamination from cosmic rays and foreground stars, we rejected point sources with compact half-light radii ($FLUX_RADIUS \leq 0''.09$ or $FLUX_RADIUS \leq -0.008 \times (MAG_AUTO - 25) + 0''.09$) in the reference images. The size criterion was visually determined on the size-magnitude diagram, which follows the horizontal sequence of point sources, with a more stringent cut applied for bright objects due to the presence of saturated stars. The numbers of all detected sources

and initially selected galaxy candidates are listed in the first and second columns of Table 4.

2.3. Photometric Redshifts and Stellar Masses

2.3.1. SED Fitting Based on eazy-py

Prior to conducting SED fitting for galaxy candidates, we carried out an aperture correction procedure to determine the total flux of each source, following the method described in Valentino et al. (2023). We measured the enclosed flux within a circular aperture with a radius of $0''.5$ and accounted for additional flux beyond the $0''.5$ aperture within the Kron radius (Kron 1980). These aperture-corrected flux values were computed from the reference images and were subsequently applied to all HST and JWST filters. We employed these aperture-corrected total fluxes for the SED analysis described in Section 2.3. To correct galactic extinctions in all HST and JWST bands, we made use of DUSTMAPS (Green 2018), with adopting a standard $R_V = 3.1$ and dust reddening maps provided in Schlegel et al. (1998).

Table 2. SExtractor Input Parameters Used for Multiwavelength Photometry

Parameter	Cold-mode Configuration	Hot-mode Configuration
DETECT_MINAREA	20	20
DETECT_THRESH	1.0	1.0
ANALYSIS_THRESH	1.0	1.0
FILTER_NAME	tophat_5.0_5x5.conv	gauss_2.5_5x5.conv
DEBLEND_NTHRESH	32	16
DEBLEND_MINCONT	0.01	0.0001
SATUR_LEVEL	100.0	100.0
BACK_SIZE ^a	64 (32)	16
BACK_FILTERSIZE ^a	5 (3)	3
BACK_PHOTOTHICK ^a	48 (24)	24 (12)

Note.

^aParameter values within parentheses are applied for the SMACS0723 field.

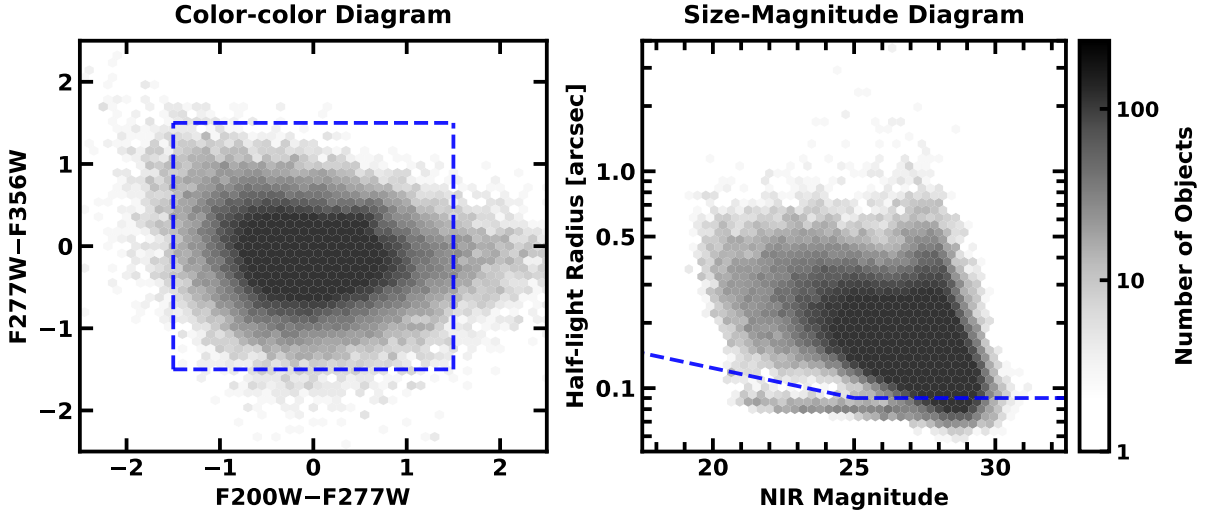


Figure 3. Left panel: Color-color diagram of the detected sources with $FLAGS \leq 4$ across all JWST fields. Measurements of $F200W - F277W$ and $F277W - F356W$ were conducted within the Kron radii of the objects. The blue dashed box denotes the selection criteria of $-1.5 < F200W - F277W < 1.5$ and $-1.5 < F277W - F356W < 1.5$ to discard artifacts. Right panel: Size-magnitude diagram of the sources, with half-light radii ($FLUX_RADIUS$) and magnitudes measured in the reference image ($F277W + F356W + F444W$). The blue dashed line represents the boundary between extended sources and point sources. Point source candidates located below this boundary were excluded from our sample for the analysis.

Photometric redshifts and stellar masses of the galaxy candidates are estimated through the SED fitting process using the EAZY-PY⁴ package (Brammer et al. 2008; Brammer 2023b). Multiwavelength fluxes measured in HST and JWST bands (see Table 1) were used for fitting the EAZY-PY model. We set the flux uncertainties to a minimum error floor of 10% to allow some flexibility in the SED fitting. We employed 14 spectral

templates from the `sfhz` model⁵, including 13 templates in the `corr_sfhz_13` subsets and an additional best-fit template from a strong emission-line galaxy observed in the SMACS0723 field (Carnall et al. 2023). Photometric redshifts were determined by identifying the redshift value corresponding to the minimum chi-square value within the range from $z = 0.05$ to $z = 12.0$, with an

⁴ <https://github.com/gbrammer/eazy-py>

⁵ <https://github.com/gbrammer/eazy-photoz/tree/master/templates/sfhz>

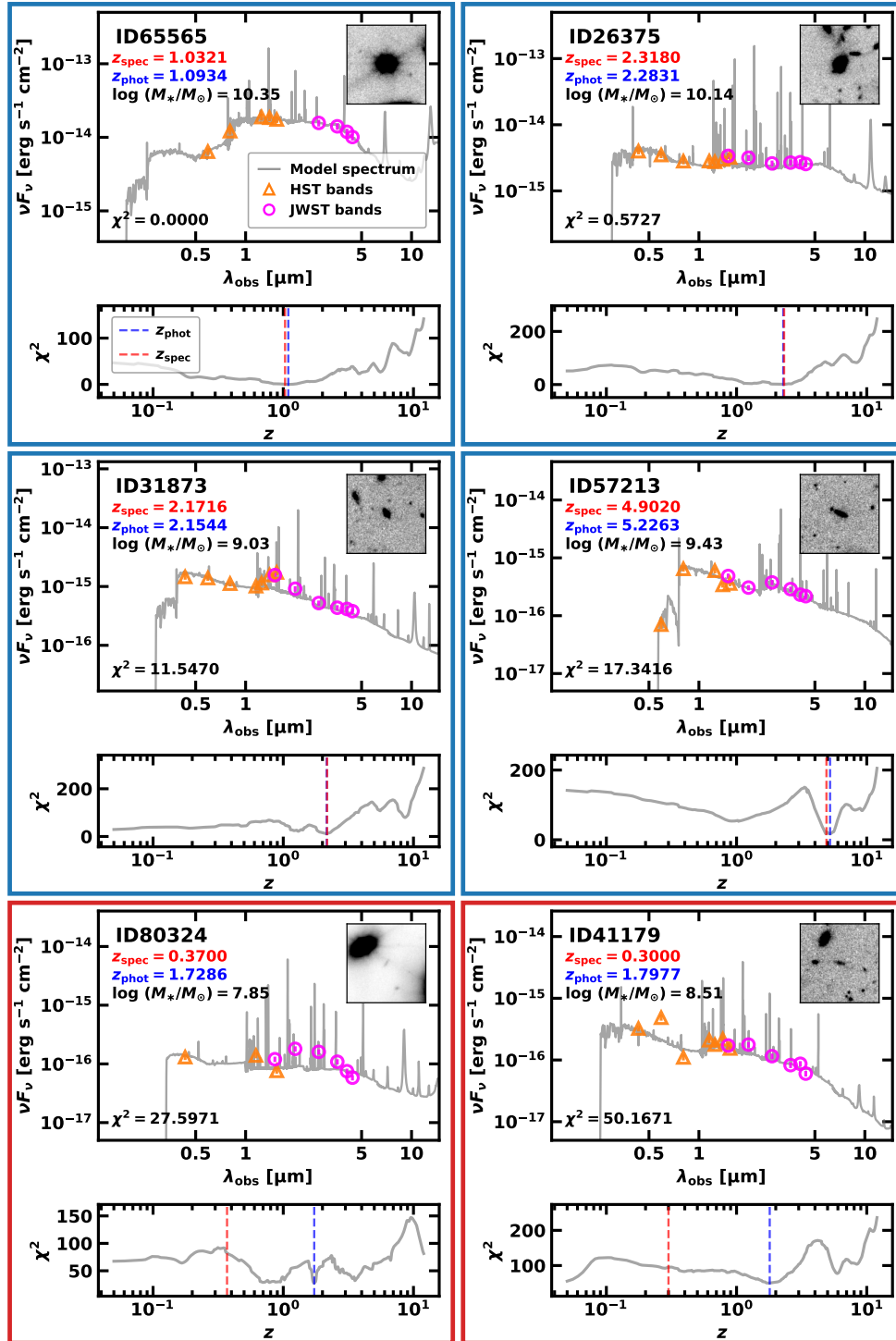


Figure 4. Examples of the SED fitting results for six galaxies in the CEERS field, ordered by their chi-square values of the best-fit EAZY-PY models. In this figure, there are three panels for each galaxy. The upper panel in each set displays the SED of the best-fit model (gray solid line) and photometric data from HST (orange triangles) and JWST (magenta circles) observations. The lower panel shows the chi-square values as a function of redshift. The spectroscopic redshift and the photometric redshift are depicted as red and blue dashed lines, respectively. A small panel on the right side displays the observed galaxy in the reference image (F277W+F356W+F444W). Based on a criterion of $\chi^2 = 20$, four galaxies in blue boxes are considered to show secure SED fitting results, while two galaxies in red boxes are thought to show unreliable results.

interval of $\log(1+z) = 0.005$. An iterative correction process for flux zeropoints was performed over 10 steps to optimize redshift values. No priors were applied on apparent magnitude and ultraviolet (UV) slope during this procedure.

After completing the SED fitting process, we evaluated the reliability of the best-fit SED models by utilizing the chi-square values (χ_{SED}^2) from EAZY-PY and the number of filters (N_{filt}) used for the SED analysis. Through visual inspection of the SED fitting results, we employed a criterion of $\chi_{\text{SED}}^2 < 20$ and $N_{\text{filt}} \geq 6$ to select well-fitted galaxy candidates. It is worth noting that our chi-square criterion is more rigorous compared to that applied in Valentino et al. (2023), which used $\chi_{\text{SED}}^2/N_{\text{filt}} \leq 8$ and $N_{\text{filt}} \geq 6$. Figure 4 illustrates examples of SED fitting results for six galaxies located in the CEERS field. Among these, four galaxies with $\chi_{\text{SED}}^2 < 20$ exhibit well-matched SEDs with their photometric data. In contrast, the best-fit SEDs for two galaxies with $\chi_{\text{SED}}^2 \geq 20$ do not align with the photometric data. These poor results might be associated with contamination from a neighboring bright galaxy (ID 80324) and the faintness of the galaxy itself (ID 41179), as seen in visual representations of the galaxies in the figure. For further analysis, we decided to exclude samples with $\chi_{\text{SED}}^2 \geq 20$ or $N_{\text{filt}} < 6$ from the EAZY-PY SED fitting.

2.3.2. Comparisons of Photometric and Spectroscopic Redshifts

In this section, we compare photometric redshifts with spectroscopic redshifts to evaluate the reliability of our photometric redshift estimations. The spectroscopic redshift data for galaxies within JWST fields were obtained from ? and the available literature. For all JWST fields, we initially obtained spectroscopic redshifts through a cone search in NED⁶. Then, the spectroscopic redshifts of galaxies in the CEERS and SMACS0723 fields were additionally sourced from Nakajima et al. (2023) and Noiro et al. (2023), which provided the redshift catalogs utilizing JWST/NIRSpec, JWST/NIRISS grism, and VLT/MUSE data. These spectroscopic sources were spatially matched with our photometric sources with $F200W < 27$ mag, allowing for a tolerance of 1".5. This tolerance was determined to consider potential offsets in the world coordinate system (WCS) between JWST images and previous data. In the NEP-TDF field, there was only one object with measured spectroscopic redshift (WISEA

J172302.06+654802.9; $z_{\text{spec}} = 0.179$), which is statistically insufficient for redshift comparisons.

Figure 5 displays the comparisons of photometric and spectroscopic redshifts from five JWST fields except for NEP-TDF. We plot the results from all matched sources in the left panel and those from the sources with stellar mass higher than $\log M_*/M_\odot > 9$, low chi-square values ($\chi_{\text{SED}}^2 < 20$), and a minimum six available filters ($N_{\text{filt}} \geq 6$) in the right panel. Outliers in this comparison were identified using the criterion of $|z_{\text{spec}} - z_{\text{phot}}|/(1 + z_{\text{spec}}) > 0.15$ (Weaver et al. 2023), which are located outside the gray dashed lines in the figure. To assess the accuracy of photometric redshifts, we also computed the normalized median absolute deviation (σ_{NMAD}) of the redshift differences ($\Delta z = z_{\text{phot}} - z_{\text{spec}}$) as defined in Equation 7 of Brammer et al. (2008). For all matched sources, the photometric redshifts of galaxy candidates show a good agreement with their spectroscopic redshifts in the redshift range from $z \sim 0.1$ to $z \sim 10$, with an outlier fraction about 11% and $\sigma_{\text{NMAD}} = 0.011$. When the stricter criterion of $\log M_*/M_\odot > 9$, $\chi_{\text{SED}}^2 < 20$, and $N_{\text{filt}} \geq 6$ is applied, the results become more reliable, yielding a lower outlier fraction of $\sim 6\%$. The performance of photometric redshift estimation slightly varies with fields, as detailed in Table 3. The outlier fractions and σ_{NMAD} values from our analysis are lower than those in previous JWST studies, which reported an outlier fraction of 10.8% and $\sigma_{\text{NMAD}} = 0.03$ in the UNCOVER survey field (Weaver et al. 2023), and $\sigma_{\text{NMAD}} = 0.018$ in the CEERS field (Valentino et al. 2023). This implies that our sample is more rigorously selected based on the SED fitting results than in previous studies.

However, it is notable that there are several sources at $z_{\text{spec}} \lesssim 1$ showing overestimated photometric redshifts with $z_{\text{phot}} \gtrsim 1$. This discrepancy can be attributed to contamination from adjacent light sources, such as blending with other galaxy light, bright background features, or bleeding light from saturated stars. These overestimated cases could be low-redshift contaminants in our analysis. To minimize these contaminants, we manually excluded a few sources close to saturated stars and bright galaxies for all JWST fields through visual inspections.

In addition, we also compared the accuracy of photometric redshifts of galaxies in the SMACS0723 field with those listed in the RELICS catalog (Coe et al. 2019). The RELICS study derived photometric redshifts using the Bayesian photoz code (BPz; Benítez 2000), with HST photometric data from optical to NIR wave-

⁶ <https://ned.ipac.caltech.edu/conesearch>

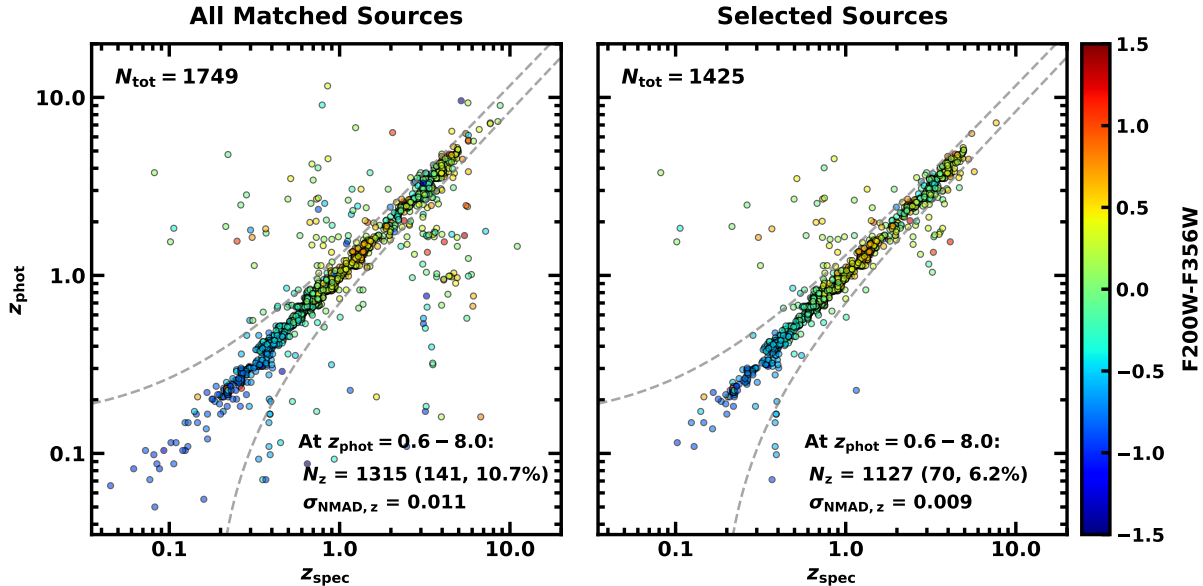


Figure 5. Comparison of photometric redshifts (z_{phot}) derived from our EAZY-PY model in this study with spectroscopic redshifts (z_{spec}) obtained from the NED and the literature. The left panel displays the comparison results for all sources, and the right panel displays the results for sources selected with $\log M_*/M_\odot > 9$, $\chi^2_{\text{SED}} < 20$, and $N_{\text{fit}} \geq 6$. Gray dashed lines indicate the criterion of $|z_{\text{spec}} - z_{\text{phot}}|/(1 + z_{\text{spec}}) = 0.15$, which is used to identify outliers. This figure provides the total numbers of sources, the numbers of outliers, the outlier fractions, and the $\sigma_{\text{NMAD}, z}$ values as text labels.

Table 3. Comparison Results of z_{phot} versus z_{spec} in Each JWST Field^{a, b}

Field	Number of Matched Sources		Number of Outliers		Outlier Fraction (%)		σ_{NMAD}
	All z	Selected z	All z	Selected z	All z	Selected z	
NGDEEP	62 (48)	42 (37)	7 (3)	4 (3)	11.3 (6.3)	9.5 (8.1)	0.007
CEERS	390 (295)	239 (207)	43 (15)	31 (13)	11.0 (5.1)	13.0 (6.3)	0.009
COSMOS	627 (531)	460 (410)	48 (23)	42 (22)	7.7 (4.3)	9.1 (5.4)	0.009
UDS	485 (392)	463 (384)	63 (29)	54 (29)	13.0 (7.4)	11.7 (7.6)	0.012
SMACS0723	185 (159)	72 (63)	16 (8)	7 (3)	8.6 (5.0)	9.7 (4.8)	0.011
Total	1,749 (1,425)	1,276 (1,101)	177 (78)	138 (70)	10.1 (5.5)	10.8 (6.4)	0.009

Notes.

^aValues in parentheses correspond to results with $\log M_*/M_\odot > 9$, $\chi^2 < 20$, and $N_{\text{fit}} \geq 6$.

^bThe selected range of redshift is $z = 1.2 - 8.0$ for SMACS0723 and $z = 0.6 - 8.0$ for the other fields.

lengths. These photometric redshifts were adopted by Ferreira et al. (2022) for investigating the morphologies of high-redshift galaxies. Figure 6 represents the comparisons of z_{phot} vs. z_{spec} both for this study (left panel) and the RELICS catalog (right panel). The RELICS sources have 180 matched objects with the spectroscopic sample from Nakajima et al. (2023) and Noirot et al. (2023), which are similar to this study. In comparison to the RELICS catalog, our photometric redshift measurements demonstrate a superior match with spectroscopic

redshifts, showing a lower outlier fraction and σ_{NMAD} . On the other hand, the RELICS catalog tends to underestimate redshifts of some galaxies at $z_{\text{spec}} > 1$, which might be due to observational limitations in HST NIR data capturing the redshifted Balmer breaks of these galaxies. These suggest that some high-redshift galaxy candidates in the SMACS0723 field might have been missed in Ferreira et al. (2022) because of underestimation of photometric redshifts in the RELICS data. Furthermore, our analysis demonstrates that the inclu-

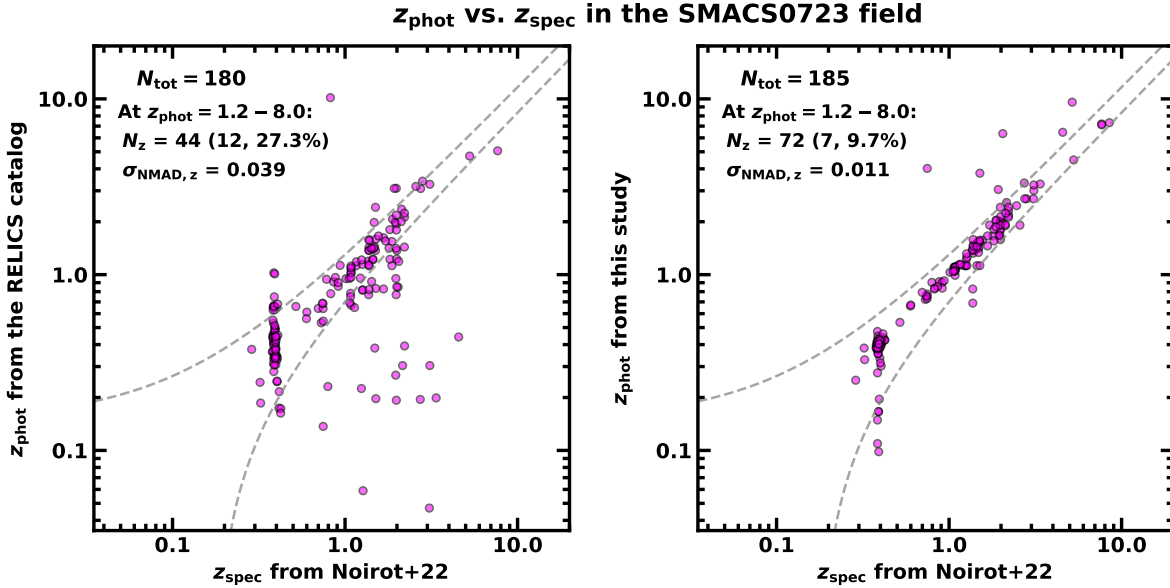


Figure 6. Comparisons of z_{phot} derived from the EAZY-PY model (left panel; this study) and the RELICS catalog (right panel; Coe et al. 2019) adopted by Ferreira et al. (2022) with z_{spec} (Nakajima et al. 2023; Noiro et al. 2023), for the sources detected in the SMACS0723 field. Gray and purple lines and texts are the same as Figure 5.

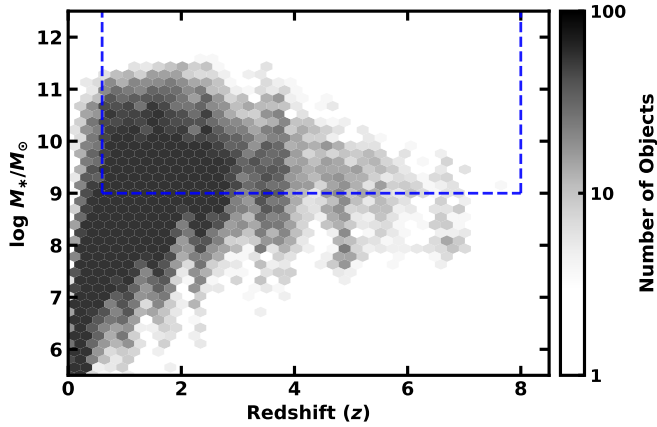


Figure 7. Distribution of stellar masses of extended sources in all JWST field as a function of redshift. Stellar masses and redshifts are derived using the EAZY-PY model in this study. The blue dashed lines represent the selection criteria of $\log M_*/M_\odot > 9$ and $z = 0.6 - 8.0$, which are used to select the galaxy candidate for morphology classification.

sion of JWST NIRCcam photometric data improves the accuracy of photometric redshifts when compared to the results obtained using HST-only data.

2.3.3. Sample Selection Based on Redshifts and Stellar Masses

This section describes our sample selection from the results of SED fitting. Initially, we established a robust sample by excluding the sources with high chi-square values ($\chi_{\text{SED}}^2 \geq 20$), smaller number of filters ($N_{\text{fit}} < 6$),

and implausible output parameters such as negative values for photometric redshift, chi-square, stellar mass, and rest-frame fluxes. In addition, we rejected faint objects with $F200W > 28$ mag from our sample due to their low signal-to-noise ratios, which could be inappropriate for the investigation of morphologies (Huertas-Company et al. 2023; Kartaltepe et al. 2023). The numbers of these robust samples from the SED fitting are listed in the third column in Table 4. We then selected the high-redshift galaxy samples for the morphological analysis based on redshifts and stellar masses. Figure 7 illustrates the stellar mass distribution for the selected objects across all JWST fields, as a function of redshift. We utilized spectroscopic redshifts when available, otherwise we employed photometric redshifts obtained through SED fitting. Our final sample for studying morphologies was chosen with a redshift range from $z = 0.6$ to $z = 8.0$ and a stellar mass range of $\log M_*/M_\odot > 9$, as represented in the figure. For the galaxies in the SMACS0723 field, we carefully selected a sample at the redshift range of $z = 1.2 - 8.0$ to minimize any potential contamination from the foreground SMACS0723 cluster. These selection criteria ensure that our sample is not significantly affected by completeness issues of observational data in the selected redshift range. The stellar mass range chosen in this study was commonly employed in most JWST studies focusing on galaxy morphology (Ferreira et al. 2023; Huertas-Company et al. 2023; Kartaltepe et al. 2023). The specific number of objects se-

lected based on redshifts and stellar masses for each field is detailed in the fourth column in [Table 4](#).

3. MORPHOLOGY CLASSIFICATION

3.1. Morphology Classification Scheme in the HR5 Study

For fair comparisons of the results on galaxy morphology among different studies, the classification scheme should be as close as possible. To ensure consistency with the HR5 study, we adopted the same morphology classification scheme described in [Park et al. \(2022\)](#). In their work, approximately 33,000 simulated galaxies with $M_* > 2 \times 10^9 M_\odot$ were categorized into three distinct types: ‘disks’, ‘spheroids’, and ‘irregulars’. As depicted in [Figure 2 of Park et al. \(2022\)](#), their classification scheme relies on two key parameters: the Sérsic index (n) and the asymmetry factor (A). These parameters were derived from the spatial distribution of stellar particles belonging to each galaxy.

In [Park et al. \(2022\)](#), symmetric galaxies were categorized with $A < 0.4$, while asymmetric galaxies were characterized by $A > 0.4$. This criterion is similar to thresholds used in previous observational studies ([Conselice 2003](#); [Ferreira et al. 2023](#); [Kartaltepe et al. 2023](#)), which differentiated undisturbed galaxies with $A < 0.35$ and merging galaxies with $A > 0.35$. However, the asymmetry measurement in [Park et al. \(2022\)](#) was based on the three-dimensional distribution of stellar particles, which could lead to a systematic difference from the asymmetry calculated using two-dimensional observational data. In this study, we adopted a criterion of $A = 0.32$ derived from the direct comparison between three- and two-dimensional asymmetry parameters (refer to [Appendix B](#) for details).

In the HR5 study, the radial stellar mass distribution within galaxies was fit by the Sérsic model. Symmetric galaxies were further divided into disks ($n < 1.5$) and spheroids ($n > 1.5$) based on the results of Sérsic profile fitting. The choice of the Sérsic index threshold of $n = 1.5$ was based on the fact that it effectively distinguishes between late-type and early-type galaxies, as elaborated in the [Appendix of Park et al. \(2022\)](#). It is very important to note that the criterion $n = 1.5$ results in the most accurate classification when the central part of galaxies is excluded in the Sérsic profile fitting as this can remove the galaxy bulge component and any observational artifact/AGN near the center. When the central part is included in the fitting, disk galaxies with a bright central bulge or core star-burst will become difficult to be distinguished from spheroidal ones.

Irregular galaxies were categorized to include asymmetric galaxies ($A > 0.32$) or galaxies where the Sérsic fitting failed. In the subsequent sections, we explain how we applied this classification scheme to categorize galaxy morphologies using JWST observational data.

3.2. Measuring the Asymmetry

The rotational asymmetry index has commonly used for quantifying the degree of asymmetry in galaxy light, as introduced by [Abraham et al. \(1996\)](#). This index is determined by calculating the sum of differences between the original image and its corresponding 180°-rotated image, relative to the sum of the original image. In [Park et al. \(2022\)](#), the asymmetry of simulated galaxies was measured using the three-dimensional stellar mass density within pixels containing at least 10 stellar particles, excluding the central region within a radius of 0.8 kpc in proper distance.

In this work, we followed a similar methodology to [Park et al. \(2022\)](#) with the additional correction for observational background noise, as recommended in [Conselice et al. \(2000\)](#) and [Lotz et al. \(2004\)](#). The asymmetry index (A) was computed using the following formula,

$$A = \frac{\sum_{i,j \in S} |I_0(i,j) - I_{180}(i,j)|}{2 \times \sum_{i,j \in S} I_0(i,j)} - A_{\text{bkg}}, \quad (1)$$

where I_0 and I_{180} are the pixel values in the original and 180°-rotated images, and A_{bkg} is the asymmetry index for the background region. The indices of i and j denote the pixels within the selected region (S) used to measure asymmetry.

To apply the formula, we followed these steps. Initially, we created cutout images for all selected galaxies with a size of $10'' \times 10''$, which is sufficient to cover the total fluxes of the galaxies. The filter selection for these cutout images was tailored to the redshift of each galaxy, as illustrated in [Figure 1](#). Then, we ran SEXTRACTOR twice on the cutout images, with a reduced background mesh size of 32, and keeping other input configurations consistent with those listed in [Table 2](#). The segmentation map from the initial SEXTRACTOR run was used to mask any neighboring light sources adjacent to the target galaxy. This masking process was implemented by replacing the pixel values of the detected contaminants with the background value of the image, creating a masked cutout image. In the second SEXTRACTOR run with the masked cutout image, we were able to more precisely measure the Petrosian radius (r_p ; [Petrosian 1976](#)) of each galaxy. We also generated a local background image around the galaxy within the masked image, by utilizing a two-dimensional linear function to fit any possible background gradients. Although the obtained JWST images were already

Table 4. Numbers of Objects in Each Field for All Selection Steps

Field	Number of objects for each step				
	(1)	(2)	(3)	(4)	(5)
NEP-TDF	12,222	4,929	2,314	799	752
NGDEEP	17,184	6,276	1,971	557	507
CEERS	86,484	44,956	13,652	5,293	5,111
COSMOS	65,430	35,620	9,829	4,119	3,982
UDS	89,178	54,101	21,729	8,793	8,412
SMACS0723	11,930	6,532	2,488	538	351
Total	282,428	152,414	51,983	20,099	19,115

Notes. Columns represent the numbers of the following source categories: (1) The total number of sources detected by `SEXTRACTOR`; (2) Extended source candidates chosen for the `EAZY-PY` SED fitting, meeting the criteria based on colors and sizes as described in Section 2.2; (3) Robust samples obtained from the `EAZY-PY` SED fitting, based on criteria such as $0 < \chi_{\text{SED}}^2 < 20$, $N_{\text{filt}} \geq 6$, $F200W < 28$ mag, and positive values for photometric redshifts, stellar masses, and rest-frame fluxes. These sources are depicted in Figure 7; (4) Galaxy candidates with $\log M_*/M_\odot > 9$ at $z = 0.6 - 8.0$; (5) The final sample selected through visual inspections and excluding non-converged sources with $n \leq \delta n$. We examine the morphologies of this final sample using `GALFIT`, as described in Section 4.

background-subtracted, these cutout images might still contain subtle background gradients. This background gradient model was used in the subsequent `GALFIT` analysis described in Section 3.3.

To calculate the asymmetry parameter, we selected a specific region for the detected source (S) within an elliptical aperture with a semi-major axis of $1.5 \times r_p$ from the galaxy center. The radius of $1.5 \times r_p$ is known to encompass nearly the total flux of a galaxy (Conselice et al. 2000; Lotz et al. 2004). The inner circular region with a radius of 0.8 kpc was excluded for this calculation, as done in Park et al. (2022). The pixel values within the region S were summed without any smoothing procedures. To correct for the background noise, we designated the background region as the area outside a radius of $1.5 \times r_p$ from the center of the galaxy. For determining A_{bkg} , we adopted the minimum asymmetry value from the background regions in the 90° -, 180° -, and 270° -rotated images. This minimum asymmetry value was then normalized by the area of the object region (S) when applying Equation 1.

3.3. Surface Photometry with `GALFIT`

We utilized `GALFIT` (Peng et al. 2002, 2010) to analyze the morphology of galaxies based on their light distribution. We used the masked cutout image of each galaxy, as mentioned in Section 3.2, as the input image for running `GALFIT`. We applied a single Sérsic profile with free parameters for the central coordinates, total magnitude, effective radius, and Sérsic index. The axis ratio and position angle were fixed to the output values derived from the second `SEXTRACTOR` run described in Section 3.2, in order to enhance the stability of `GAL-`

`FIT` solutions and speed up the fitting procedure. In addition, we applied a two-dimensional sky component with a free sky background value and fixed sky gradients along the x and y axes.

It is important to note certain limitations in our choice of a single Sérsic profile for `GALFIT` in this study. Galaxies are known to exhibit multiple morphological components such as disks, bars, spiral arms, bulges, and irregular features resulting from merger or tidal processes. In particular, around 10% of galaxies have both bulge components ($n \sim 4$) at their centers and exponential disk components ($n \sim 1$) in their outskirts simultaneously (Huertas-Company et al. 2023; Kartaltepe et al. 2023). This inherent complexity in galaxy morphology has led previous studies on high-redshift galaxy morphology to rely on visual classification and use parametric measurements from `GALFIT` as a supplement. Ideally, the inclusion of multiple Sérsic profiles in the `GALFIT` configurations would be more beneficial for tracing the detailed morphological structures of real galaxies. However, multiple Sérsic fitting does not work effectively for most high-redshift galaxies with small apparent size ($R_{\text{eff}} \lesssim 0''.2$), and it is very challenging to apply to a large sample of galaxies. Therefore, this work opted to use a single Sérsic profile for the consistency in methodology with the HR5 study and the convenience of analyzing a large sample of high-redshift galaxies.

In our `GALFIT` configurations, we employed point spread function (PSF) images generated from `WEBBPSF` (Perrin et al. 2014) to account for the PSF effect. We resampled the PSF images of NIRCcam bands to the pixel scale of $0''.04 \text{ pixel}^{-1}$, with the image sizes

of $5'' \times 5''$. The size of the PSF convolution box was set to be larger than the total area of the input images. Since WEBBPSF only creates the simulated PSFs of JWST/NIRCam, it is necessary to test the effect of empirical PSF models which can reflect the quality of real drizzled images (Ono et al. 2023; Zhuang & Shen 2024). For this reason, we also generated empirical PSFs utilizing PSFEX (Bertin 2011) and applied them to the GALFIT analysis of the whole sample. We found that the choice of PSF models have little influence on our main results in Section 4.2. We described the details of the tests for empirical PSFs in Appendix C.

To minimize the cases of obtaining unreasonable results, we imposed constraints on the Sérsic index, ranging from 0.2 to 10, and the coordinate offsets to $0''.1$ (2.5 pixels) from the galaxy center. After executing GALFIT, we systematically rejected sources with unreliable solutions, with the uncertainty of the Sérsic index (δn) exceeding the value of the Sérsic index itself ($n \leq \delta n$). The final sample size with this rejection is detailed in the fifth column of Table 4.

We evaluated the quality of the GALFIT fitting by computing the residual flux fraction (RFF ; Hoyos et al. 2011) for each galaxy. The RFF measures the signal in a residual image relative to the sum of the original image. As in Hoyos et al. (2012), the RFF is defined as,

$$RFF = \frac{\sum_{i,j \in S} |I(i,j) - I(i,j)^{\text{model}}| - 0.8 \times \sum_{i,j \in S} \sigma_B(i,j)}{\sum_{i,j \in S} I(i,j)} \quad (2)$$

where $|I(i,j) - I(i,j)^{\text{model}}|$ is the residual signal between the input image and the GALFIT model image. σ_B denotes the background fluctuation, and S is the region selected for this calculation. In this study, we selected S as an elliptical region within a semi-major axis of $1.5 \times r_p$, excluding the central region within a radius of 0.8 kpc. In terms of the background fluctuation, we adopted the background sigma for the total area of the masked cutout image, as assumed in Margalef-Bentabol et al. (2016). The equation used for calculating the background fluctuation is as follows,

$$\sum_{i,j \in S} \sigma_B(i,j) = N_S \times \langle \sigma_B \rangle, \quad (3)$$

where N_S is the number of pixels belonging to the area used for RFF calculation, and $\langle \sigma_B \rangle$ is the mean background sigma in the image. We determined $\langle \sigma_B \rangle$ to be the clipped sigma value from the region outside the Petrosian aperture (S).

We utilized the RFF as a proxy to assess the success of a single Sérsic fitting. The specific RFF criterion has not been agreed well because it can vary depending on

the quality of observational data and the scientific purposes of using the RFF . In a recent JWST study by Ormerod et al. (2023) and Ward et al. (2023), the RFF was employed as a criterion for excluding poorly-fit objects with $RFF > 0.5$. This threshold was found to be more generous than previous HST studies, which suggested that objects with $RFF > 0.11$ are needed to fit with additional Sérsic components (Hoyos et al. 2011), or merger candidates could be effectively found with $RFF > 0.2$ (symmetric cases) or $RFF > 0.1$ (asymmetric cases). In this work, we adopted the criterion of $RFF > 0.5$ to identify obviously poorly-fit objects from the GALFIT analysis along with avoiding any misclassification of multi-Sérsic objects as poorly-fit ones.

3.4. Parametric Morphological Classification in This Study

Utilizing the results obtained from asymmetry measurements and GALFIT fitting, we applied the following parametric criteria for morphology classification:

- (1) Disk-type galaxies: $n < 1.5$, $A < 0.32$, and $RFF < 0.5$,
- (2) Spheroid-type galaxies: $n > 1.5$, $A < 0.32$, and $RFF < 0.5$,
- (3) Irregular-type galaxies: $A > 0.32$ or $RFF > 0.5$.

Symmetric and well-fitted galaxies with $A < 0.32$ and $RFF < 0.5$ were further categorized into disk-type ($n < 1.5$) and spheroid-type galaxies ($n > 1.5$) based on their Sérsic indices. Irregular-type galaxies in our analysis encompass both asymmetric galaxies with $A > 0.32$ and poorly-fit galaxies with $RFF > 0.5$. This parametric classification scheme is consistent with the criteria applied in Park et al. (2022).

Figure 8 illustrates the examples of our morphological classification. Disk galaxies in the top two panels show nearly exponential light profiles ($n \sim 1$), occasionally accompanied by spiral arm structures (ID 22014). Spheroid galaxies in the middle two panels are characterized by bulge-like structures with higher Sérsic indices ($n \gtrsim 2$) compared to disk galaxies. In the bottom two panels, irregular galaxies exhibit more remarkable substructures in their residual images compared to disks and spheroids. Although there could be a potential problem of misjudgement near the sharp classifying boundary of parameters, our parametric classification scheme generally aligns with the common visual classification of galaxy morphology for the majority of galaxies in our extensive sample.

4. RESULTS

4.1. Distributions of Asymmetry, RFF , and Sérsic indices

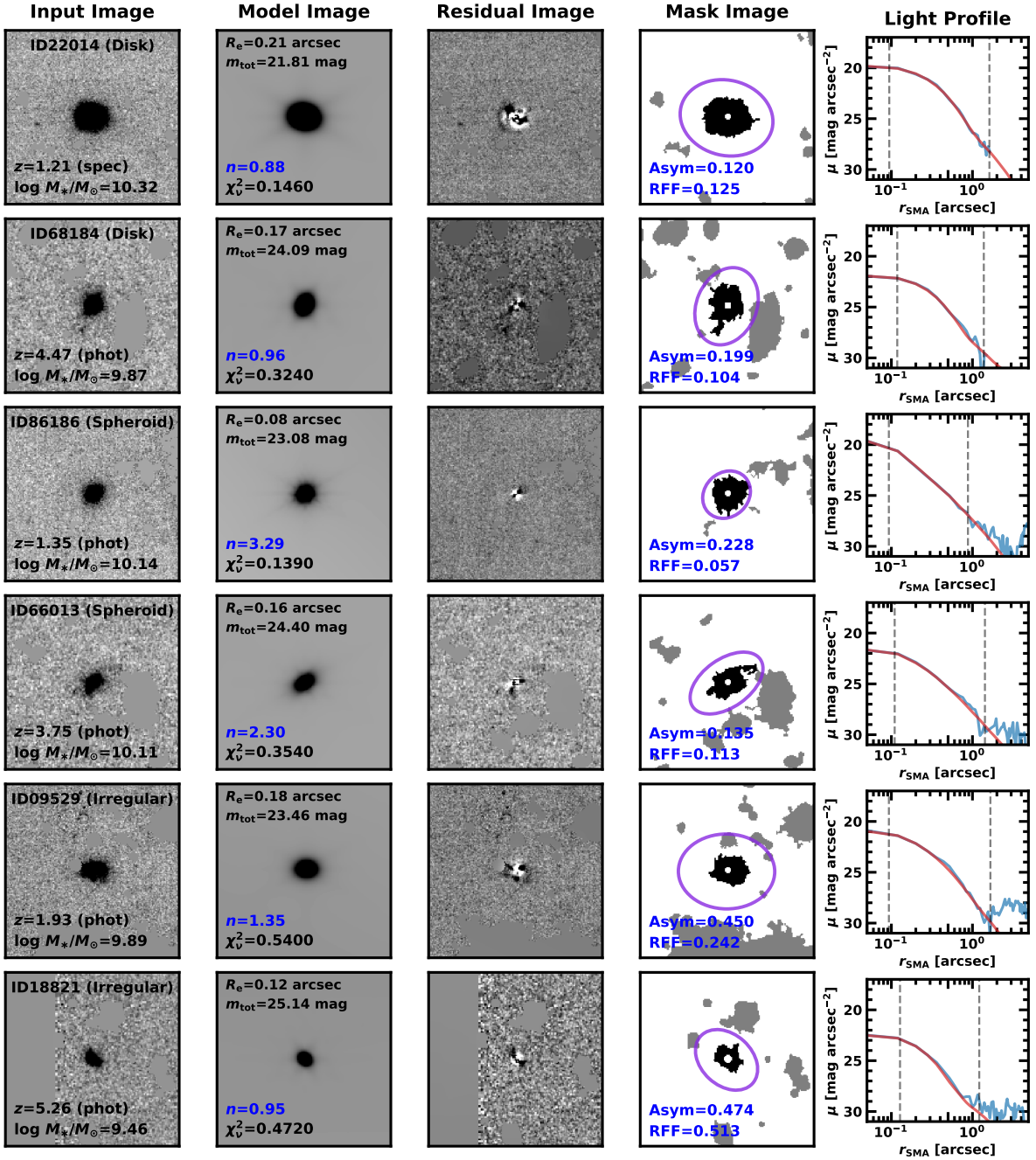


Figure 8. Thumbnail images ($6'' \times 6''$) of high-redshift galaxies selected in this study. The examples include six galaxies, with two galaxies in each morphological category: disks (upper two objects), spheroids (middle two objects), and irregulars (lower two objects). Each galaxy example is represented by five panels. The leftmost panels display the masked cutout images used as input for GALFIT. The subsequent two panels display the model images and residual images obtained from GALFIT. In the fourth panels, the mask images show the distribution of masked pixels in the gray region, with the black region representing the 1σ boundary of light from objects recorded in the segmentation map. Purple ellipses represent apertures with a semi-major axis of $1.5 \times r_p$ of each galaxy. The fifth panels show the radial light profiles measured from the galaxy center to the image edge. Original light profiles are depicted by blue curves, while the model light profiles from GALFIT are depicted by red curves. The two gray dashed lines represent a semi-major axis corresponding to 0.8 kpc (left) and a semi-major axis of $1.5 \times r_p$ of the galaxy (right). Key parameters for morphology classification are denoted by blue texts in this figure.

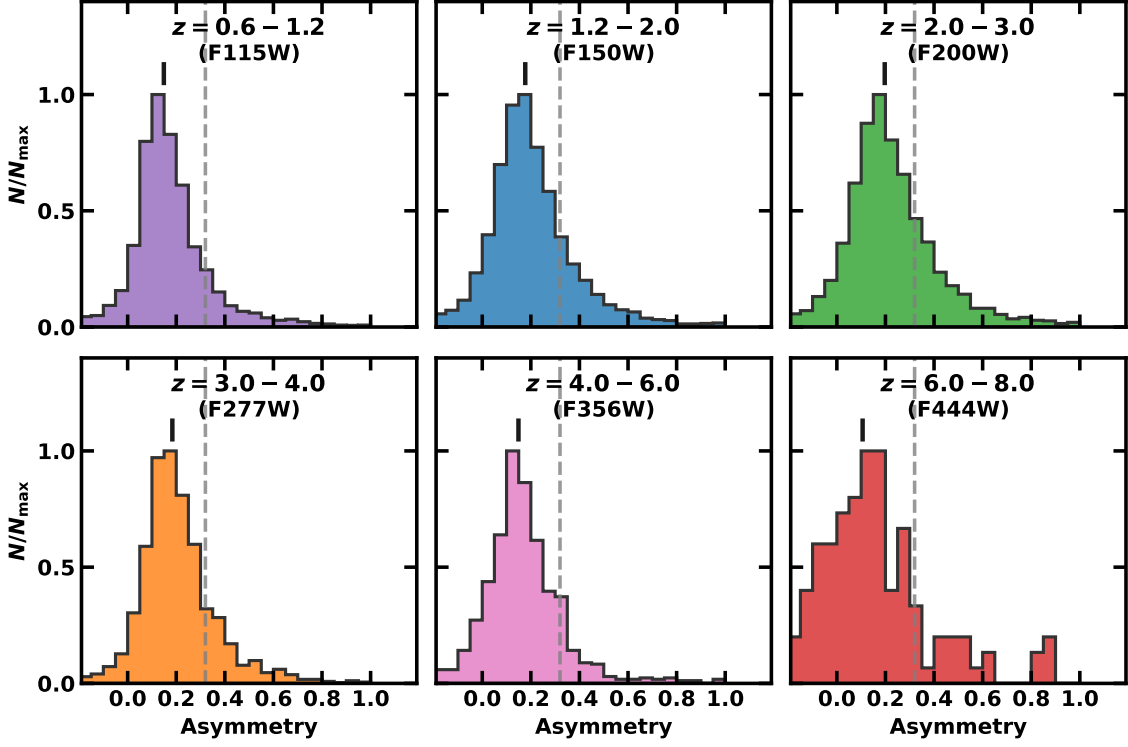


Figure 9. Histograms depicting the asymmetry of galaxies in all JWST fields. The panels are organized based on the chosen JWST/NIRCam filters corresponding to the respective redshift ranges. The gray dashed lines represent our criterion to distinguish symmetric ($A < 0.32$) and asymmetric ($A > 0.32$) galaxies. The black lines mark the median values of asymmetry in each redshift bin.

Table 5. Statistics of asymmetry, RFF , and Sérsic index of Galaxies in Each JWST Field

Field	Asymmetry		RFF		Sérsic index	
	Median	σ_{MAD}	Median	σ_{MAD}	Median	σ_{MAD}
NEP-TDF	0.18	0.11	0.14	0.11	1.06	0.39
NGDEEP	0.24	0.09	0.24	0.08	1.06	0.37
CEERS	0.19	0.08	0.16	0.09	1.09	0.40
COSMOS	0.17	0.09	0.12	0.09	1.09	0.41
UDS	0.16	0.09	0.08	0.10	1.06	0.40
SMACS0723	0.20	0.10	0.16	0.12	1.03	0.37
Total	0.18	0.09	0.12	0.10	1.08	0.40

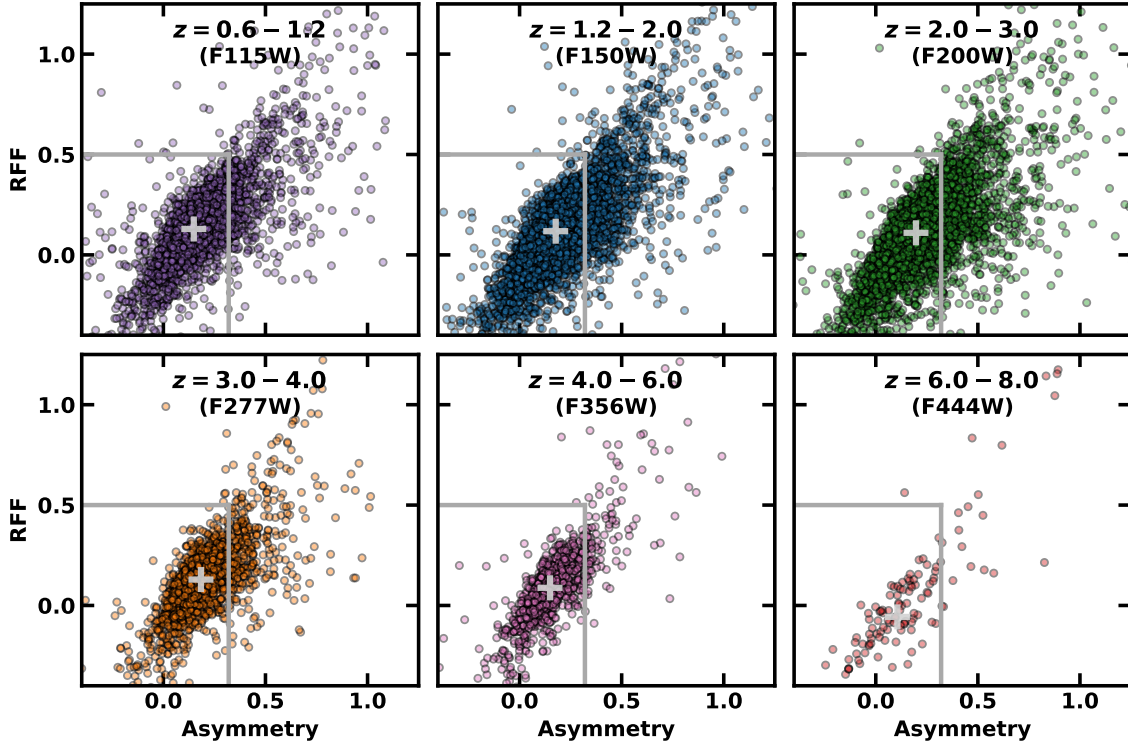


Figure 10. Distributions of asymmetry and RFF values of our sample. The panels are ordered as in [Figure 9](#). The gray lines denote the selection criteria of $RFF = 0.5$ and $A = 0.32$ to divide regular galaxies (disks and spheroids) and irregular galaxies in this study. The gray cross symbols mark the median values of RFF and asymmetry in each redshift bin.

In this section, we present the distributions of key parameters for morphology classification: asymmetry, RFF , and Sérsic indices. [Figure 9](#) shows the distributions of asymmetry values of our sample galaxies. The asymmetry distributions exhibit a strong concentration around $A \sim 0.18$ across all redshift ranges. As also shown in [Table 5](#), the median asymmetry values of galaxies in each JWST field are also around $A \sim 0.18$, indicating no systematic biases in asymmetry measurements depending on filters and fields. [Figure 9](#) also shows elongated tails towards higher asymmetry values in all redshift ranges. These tails are indicative of irregular galaxies with mergers and remarkable substructures. As mentioned in [Section 3.1](#), we classified galaxies as asymmetric when $A > 0.32$, which is consistent with the criterion of three-dimensional asymmetry with $A > 0.4$ in [Park et al. \(2022\)](#).

[Figure 10](#) displays the distributions of RFF and asymmetry in each redshift range. We note that there is a positive correlation between RFF and asymmetry, implying that asymmetric galaxies have high residual fluxes from a single Sérsic fitting. The RFF distributions consistently show median values of $RFF \sim 0.12$ at

$z < 4$, whereas at $z > 4$, the median RFF values become lower than 0.1. This decrease in RFF at higher redshifts might be due to the reduced effective radii in both physical and angular sizes of galaxies in the early universe. In contrast to asymmetry, there are some systematic variations in RFF values of galaxies depending on the JWST fields, as shown in [Table 5](#). These field-to-field variations result from differences in background fluctuations within the images of the JWST fields. For instance, the NGDEEP field shows relatively higher RFF with a median value of 0.24 and $\sigma_{MAD} = 0.08$, compared to other fields with a median value of 0.12 and $\sigma_{MAD} = 0.10$. This is because the JWST images of NGDEEP have a deeper surface brightness limit, leading to lower background sigma in [Equation 2](#). However, these systematic variations across JWST fields have a negligible effect when applying the generous criterion of $RFF > 0.5$ to identify poorly-fit galaxies. In addition, a majority of galaxies classified as irregulars are selected with the asymmetry criterion of $A > 0.32$, so the $RFF > 0.5$ criterion has an insignificant effect on the classification of irregular galaxies.

[Figure 11](#) displays the distribution of Sérsic index as a function of stellar mass and redshift. Although we applied the $n = 1.5$ criterion to classify disk and

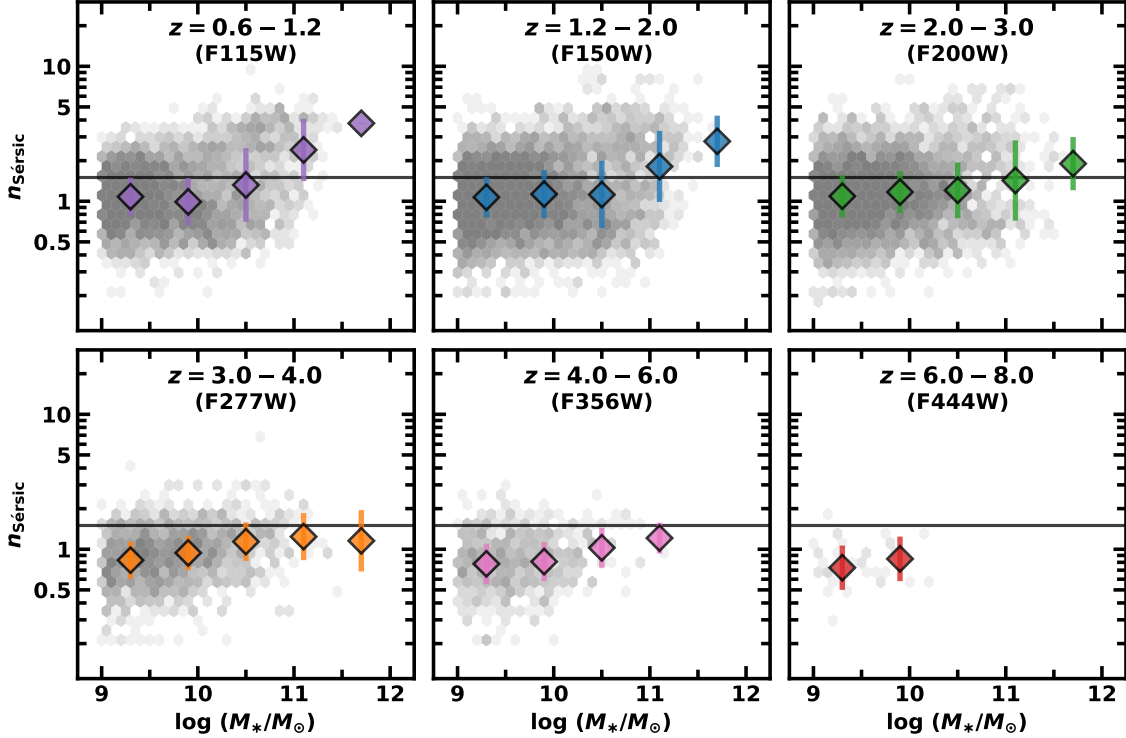


Figure 11. Distributions of Sérsic indices as a function of stellar mass. The panels are ordered as in [Figure 9](#). The median values of Sérsic indices in each stellar mass bin are represented by diamond symbols, along with their deviations. The black dashed lines mark the criterion of $n = 1.5$ to distinguish disk galaxies and spheroid galaxies. In this figure, we do not plot median values for stellar mass bins with fewer than five objects.

spheroid galaxies, our analysis reveal continuous distributions of Sérsic indices across all redshift ranges. The reason of our choice of $n = 1.5$ is described in [Section 3.1](#) and the [Appendix of Park et al. \(2022\)](#). Overall, Sérsic indices tend to increase in the high-mass regime of $\log M_*/M_\odot \gtrsim 10.5$, indicating that galaxy mass growth via mergers is accompanied by bulge-like structures with higher Sérsic indices. Examining the redshift evolution of Sérsic indices, we find that galaxies at $z > 3$ exhibit slightly lower Sérsic index compared to those at $z < 3$. With our classification framework, spheroid galaxies with $n > 1.5$ appear more dominant than disk galaxies in the $\log M_*/M_\odot \gtrsim 10.5$ range at $z < 3$ and become rare at $z > 3$. As shown in [Table 5](#), the distribution of Sérsic index is statistically consistent across all the JWST fields with a very small field-to-field fluctuation of the median n .

4.2. Morphological Distribution with Stellar Mass and Redshift

Here, we explain the morphological fractions in various stellar mass and redshift ranges, utilizing data collected from all six JWST fields. It is worth noting that, unlike the other five blank fields, SMACS0723 has a dense galaxy cluster at $z = 0.39$. This may lead to sig-

nificant interference from bright light emitted by cluster members and the intracluster medium. In addition, the gravitational lensing effect induced by the SMACS0723 cluster can magnify and distort the morphologies of high-redshift galaxies. Despite these potential problems, the general trends of morphological fractions from the small sample of the SMACS0723 field seem to be quite consistent with those in other fields (see [Appendix A](#)). Thus, we use the data from the SMACS0723 field for [Figures 12, 13, and 14](#), with only excluding galaxies at $z = 0.6 - 1.2$.

[Figure 12](#) shows morphological fractions relative to stellar mass in redshift bins corresponding to different JWST filters. To calculate uncertainties in each bin, we considered both Poisson noise from the sample size and field-to-field variations in morphological fractions. Detailed information on morphological fractions for each JWST field is provided in [Appendix A](#), along with the calculation method for uncertainties. [Figure 12](#) reveals a clear dependence of disk and spheroid fractions on stellar mass. In the $\log M_*/M_\odot < 10$ mass regime, disk galaxies are dominant constituting $\gtrsim 60\%$ at all redshift ranges. Spheroid fractions increase with stellar masses at all redshifts. At $z < 3$, spheroid galaxies

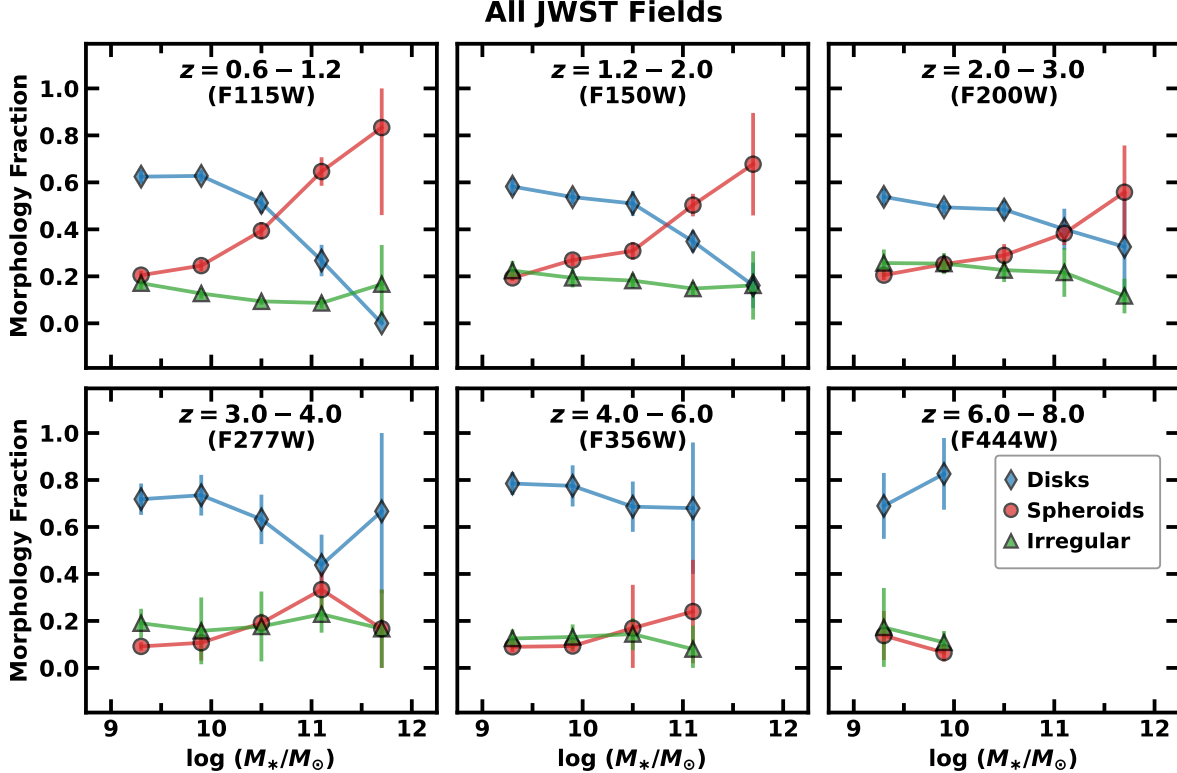


Figure 12. Morphological fractions as a function of stellar mass in various redshift bins. The fractions of disks, spheroids, and irregulars are denoted by blue diamonds, red circles, and green triangles, respectively. We plot the data from all six JWST fields. We do not plot the fractions for stellar mass bins with fewer than five objects.

become dominant in the high-mass regime, specifically $\log M_*/M_\odot > 10.5$ at $z < 2$ and $\log M_*/M_\odot > 11$ at $z = 2 - 3$. Beyond $z > 3$, spheroid galaxies consistently show lower proportions than disk galaxies across all stellar mass ranges. Nevertheless, increasing trends in spheroid fractions still appear from the mass range of $\log M_*/M_\odot \gtrsim 10$. In the case of irregular galaxies, their fractions remain nearly constant at around 20% in all ranges of stellar mass and redshift.

We plot the combined data of morphological fractions in relation to stellar mass and redshift in **Figure 13**. The left panel shows the dependence of morphological fraction on stellar mass, combining data at all redshift ranges. As stellar mass increases, the disk fraction decreases and the spheroid fraction increases; the crosspoint of disk and spheroid fractions occurs around $\log M_*/M_\odot \sim 10.5 - 11.0$. The irregular fraction is nearly independent on stellar mass but slightly increases as stellar mass decreases in the range of $\log M_*/M_\odot < 11$, showing a larger fraction than spheroid fraction at $\log M_*/M_\odot \lesssim 10$. The right panel shows the morphological fractions with redshifts, providing an insight on cosmic evolution of galaxy morphology. In the early universe at $z > 3$, disk galaxies are a little more prevalent

than at $z < 3$, with a fraction of $\gtrsim 70\%$ compared to $\sim 60\%$ at $z < 3$, while spheroid fraction increases at this cosmic period. This is due to the mass dependence of galaxy morphology and the fraction of massive galaxies increases at lower redshifts. The spheroid fraction is only $\sim 10\%$ at $z > 3$, but reaches $\gtrsim 20\%$ at $z < 2$. Irregular fraction does not show a monotonic relation with redshifts. The irregular fraction seems to reach a maximum during the cosmic noon, $z = 2.0 - 3.0$.

The dominance of disk galaxies at high redshifts and at relatively low stellar mass implies that the initial morphology of galaxies is disk-like when they first form. Spheroidal and irregular galaxies also exist beyond $z > 3$, but these galaxies constitute only about 10 – 20%. Changes in morphological fractions with stellar mass and redshift suggest that spheroid and irregular galaxies can be formed from initial disk galaxies via mergers or interactions. In the redshift range of $z \lesssim 2$, some of irregular galaxies seem to evolve into disk or spheroid galaxies, leading to a decrease in irregular fraction.

5. DISCUSSION

5.1. Comparison with the HR5 Results

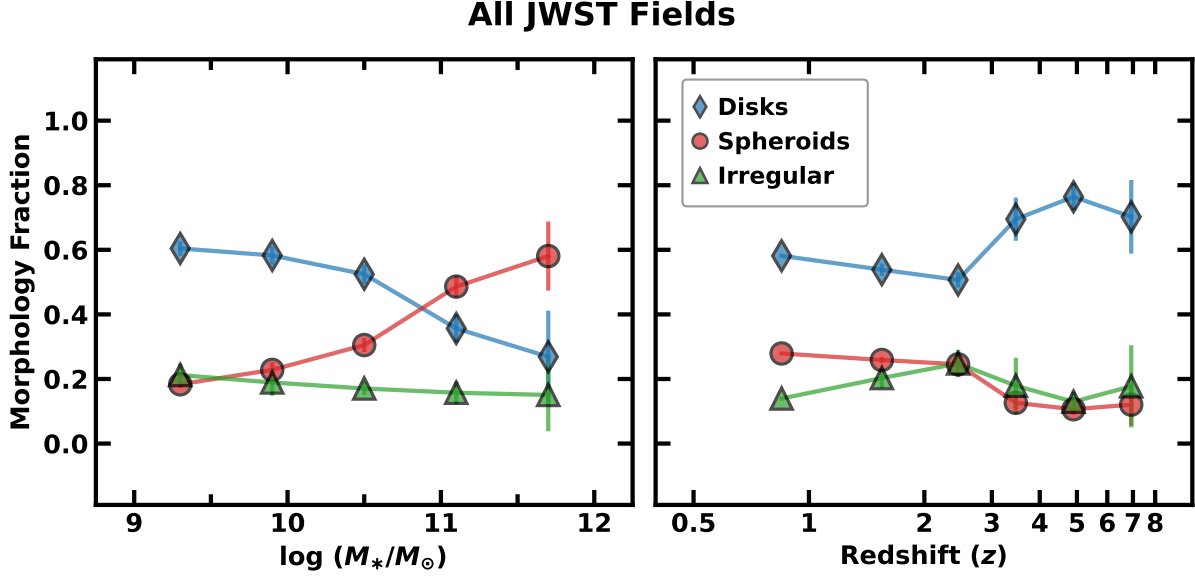


Figure 13. Morphological fractions as a function of stellar mass (left panel) and redshift (right panel). Symbols are the same as [Figure 12](#). Here we also collect the data from all six JWST fields.

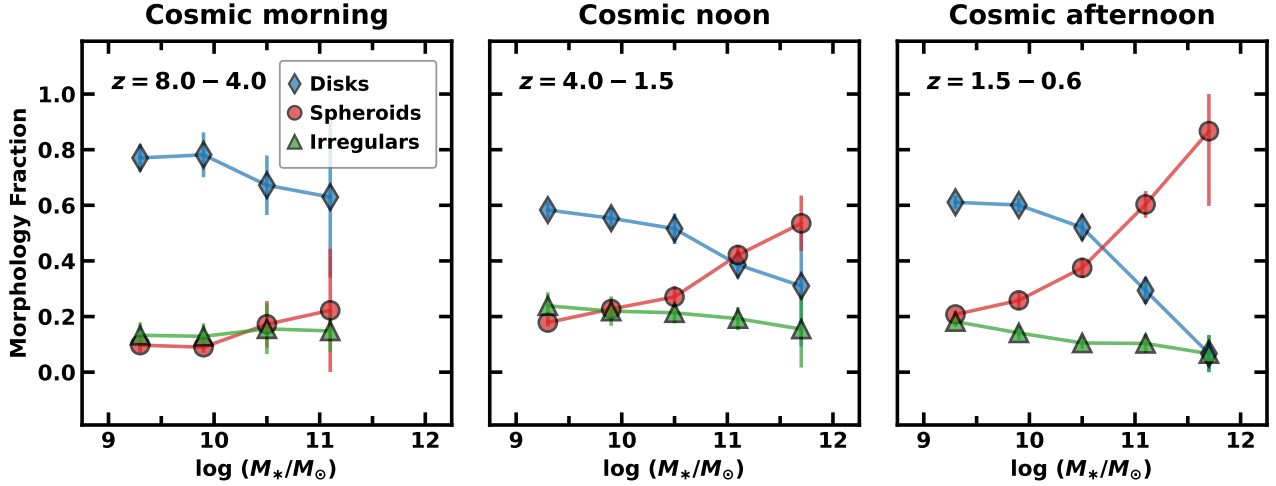


Figure 14. Morphological fractions as a function of stellar mass at cosmic afternoon ($z < 1.5$; left panel), cosmic noon ($z = 1.5 - 4.0$; middle panel), and cosmic morning ($z > 4$; right panel). Symbols are the same as [Figure 12](#). As in [Figure 12](#), we do not plot the fractions for stellar mass bins with fewer than five objects.

Our results on the morphology fraction of high-redshift galaxies agree closely with those of [Park et al. \(2022\)](#) in many ways. It should be noted that [Park et al. \(2022\)](#)'s prediction had been presented before any JWST results were announced. In the HR5 simulation, about 70% of the first galaxies with $9.3 < \log M_*/M_\odot \lesssim 10$ are found to have disk morphology at $z > 4$ (refer to their Figure 11). The rests are divided into irregulars and spheroids more or less equally. Spheroid and irregular fractions are nearly independent of redshift and stellar mass within the mass range, each type consti-

tuting around $\sim 1/6$ of the first galaxies. For comparison with these HR5 results, we depict the morphological fractions with stellar mass in [Figure 14](#), categorizing the cosmic epochs of ‘cosmic morning ($z > 4$)’, ‘cosmic noon ($z = 1.5 - 4$)’, and ‘cosmic afternoon ($z < 1.5$)’, following [Park et al. \(2022\)](#)'s definition.

The left panel of [Figure 14](#), showing the morphological fraction of the three galaxy types in the cosmic morning ($z > 4$), illustrates a stunning agreement between our JWST observational results and HR5 cosmological simulation predictions. This panel shows that

disk galaxies account for about 75% of galaxies with $\log M_*/M_\odot \lesssim 10$ at $z > 4$, while spheroid and irregular galaxies account for about 10% and 15%, respectively. These morphological distributions closely resemble those from the HR5 study, indicating that the theoretical predictions on the morphology of the first galaxies by HR5 are clearly supported by our JWST results.

In one of the HR5 snapshots during the cosmic noon period ($z \sim 2$), disk galaxies remain dominant, comprising around $\sim 70\%$ of galaxies in the $\log M_*/M_\odot \lesssim 10$ range (refer to Figure 20 in Park et al. (2022)). However, the disk fraction shows a sharp decline in the mass range $\log M_*/M_\odot \gtrsim 10.5$. Meanwhile, the spheroid fraction surpasses disk fraction in the $\log M_*/M_\odot > 11$ range, and irregular fraction also reaches up to $\sim 35\%$ at $\log M_*/M_\odot \gtrsim 10.5$. These trends of disk and spheroid fractions in the HR5 simulation also appear in a very similar fashion in our JWST analysis, as demonstrated in the middle panel of Figure 14. The results from this study show disk dominance up to $\log M_*/M_\odot \sim 11$ and spheroid dominance at higher masses. However, the irregular fraction in our observational study shows a somewhat different behavior from that in the HR5 simulation. The fraction indeed reaches a maximum during the cosmic noon period, but is nearly constant with $\sim 20\%$ regardless of stellar mass, in contrast to the jump at $\log M_*/M_\odot = 10 - 10.5$ found by Park et al. (2022). This discrepancy could arise from differences in irregular classifiers, such as asymmetry and *RFF*, which may not be matched perfectly with those used in the HR5 study.

Morphological fractions in the cosmic afternoon ($z < 1.5$) in the right panel of Figure 14 provide an insight on the morphological evolution of galaxies from high redshifts ($z > 4$) to $z \lesssim 1$. It seems that the disk fraction in the cosmic afternoon has not changed much since the cosmic noon. On the other hand, the spheroid fraction shows a noticeable increase, reaching $\sim 70\%$ in the high-mass regime ($\log M_*/M_\odot > 11$). The irregular fraction in the cosmic afternoon exhibits a gentle decline with increasing stellar mass, in contrast to the constant fraction of $\sim 20\%$ in the cosmic noon. These trends in spheroid and irregular galaxies suggest that massive irregular galaxies in the cosmic noon or morning are likely to evolve into spheroid galaxies as they kinematically settle down and maintain the spheroidal morphology.

In summary, we note the following points from the perspective of these three cosmic periods. First, disk galaxies are dominant in the cosmic morning with the fraction of $\sim 75\%$ for those with $\log M_*/M_\odot \lesssim 10$, implying that disks are the initial morphology of the first galaxies. Second, morphological transformations

from disks to spheroids or irregulars occur across all the cosmic epochs, particularly in the mass range of $\log M_*/M_\odot \gtrsim 10.5$. Third, spheroid galaxies exist in the cosmic morning at relatively low masses, but dominates the galaxy population in the cosmic noon and afternoon in the high-mass regime of $\log M_*/M_\odot \gtrsim 10.5 - 11$. Fourth, the irregular fraction increases from the cosmic morning to the cosmic noon but decreases again in the cosmic afternoon due to the reduced number of massive irregular galaxies. Lastly, these trends of morphological fractions can imply an evolutionary sequence from disks to spheroids or irregulars, with massive irregular galaxies eventually transforming into spheroids in the cosmic afternoon. Overall, these findings align very well with the morphological evolution of galaxies suggested in the HR5 simulation.

5.2. Formation and Evolution of Disks from the Early Universe

In this study, we observed a prevalence of disk-type morphology for the galaxies with stellar masses $\log M_*/M_\odot \lesssim 10$ at $z > 4$, which aligns with the HR5 results. Interestingly, our findings from JWST images, capturing the distribution of stellar light, exhibit a good agreement with the HR5 simulation based on stellar mass distribution. Park et al. (2022) explained that the emergence of disk-type morphologies in the early universe can be attributed to the initial angular momentum in protogalactic clouds. The initial angular momentum is gained from the inflow of cold gas into protogalaxies along primordial large-scale structures, which is consistent with the basis of the tidal torque theory (Peebles 1969; White 1984). According to this theory, the tidal field on protogalactic regions and corresponding velocity field are governed by the large-scale dark matter distribution, which keep galaxies to acquire angular momentum set up by the initial conditions. The competition between the tidal torque driving galaxies into disk type and mergers driving galaxies into irregulars and spheroids determines the morphology distribution. The dominance of disks in the cosmic morning can be elucidated with these underlying physical processes.

In Figure 14, our analysis reveals $\sim 20\%$ decrease in disk fraction at small masses during the cosmic noon and afternoon compared to the cosmic morning, in contrast to a notable increase in the spheroid fraction in the high-mass regime. In the low-mass regime ($\log M_*/M_\odot < 10$), there is a slight increase of 5 – 10% in the irregular fraction from the cosmic morning to the cosmic noon, indicating a tendency for disk galaxies in this mass range to transform into irregular galaxies.

However, it is important to note that mergers do not inevitably lead to irreversible morphological changes from disks to other types. Despite undergoing morphological transformations due to mergers or destructive interactions, the initial disk structures can be restored through the acquisition of angular momentum via gas accretion from the vorticity-rich surrounding matter (Welker et al. 2014; Park et al. 2022). Indeed, the HR5 simulation supported this recovery process, demonstrating morphological fluctuations in initial disk galaxies with changing Sérsic indices (refer to Figure 12 in Park et al. 2022). Consequently, this disk recovery mechanism can effectively explain why the disk fraction remains high in the cosmic morning in spite of high merger rate at corresponding redshifts (Duncan et al. 2019).

5.3. Comparison with Other Observational Studies on Galaxy Morphology

For comparison with other observational studies, it is important to note that the morphology classification schemes employed in other studies are not consistent with ours. We applied the parametric classification described in Section 3.4 for consistent comparison with the HR5 study, but previous studies have used different morphology classification approaches with various scientific objectives. Commonly employed methods are visual classification with measurements of CAS parameters or machine learning techniques applied to large datasets. Thus, the direct comparison with other studies is difficult. Furthermore, our parametric classification has a potential problem of misclassifying the galaxies with parameters around $n \sim 1.5$ or $A \sim 0.32$ as our classification adopts sharp boundaries. Despite these systematic differences and limitations, we discuss both agreements and disagreements on morphological distribution and evolution with the results from previous studies.

Most studies using HST data disagree with our findings of disk dominance in the early universe. Previous HST studies have suggested a prevalence of irregular galaxies with disturbed structures at $z \gtrsim 4$, rather than the disk dominance (Papovich et al. 2005; Cameron et al. 2011; Mortlock et al. 2013; Huertas-Company et al. 2016). Otherwise, a few studies have demonstrated high spheroid fractions of $\sim 30\%$ at $z \gtrsim 2$ in the rest-frame UV wavelength (Lotz et al. 2006; Dahlen et al. 2007). These discrepancies with our results may arise from the limited observational performance of HST for high-redshift galaxy morphology and differences of observing wavelength ranges in the rest frame. This is also pointed out by several JWST studies, which suggested that results based on JWST images exhibit a higher incidence of regular morphologies, such as disks and

spheroids, compared to HST (Ferreira et al. 2022; Jacobs et al. 2023). Furthermore, JWST images are useful for uncovering hidden disk galaxies within the noise of HST images (Nelson et al. 2023; Robertson et al. 2023).

Recent JWST studies agree with our findings regarding disk dominance in the early universe. Ferreira et al. (2022, 2023), utilizing visual classification with JWST fields of the SMACS0723 and CEERS, reported that disk galaxies occupy 40 – 60% of the entire galaxy population at $z = 1.5 - 6.5$. They found that the disk fraction increases by a factor of 10 when using JWST images compared to investigations based solely on HST images. The spheroid and irregular fractions are nearly constant at 10 – 20%, 30 – 40%, respectively, with respect to redshifts. Kartaltepe et al. (2023), also employing visual classification in the CEERS field, presented a dominant disk fraction of $\sim 60\%$ at $z \sim 3$, declining to $\sim 30\%$ beyond $z > 6$. Similar to our results, Kartaltepe et al. (2023) noted an increase in spheroid fraction in the high-mass regime ($\log M_*/M_\odot \gtrsim 10.5$) across all redshift ranges. They reported pure spheroid and irregular fractions of $\sim 20\%$ at $z > 3$, with a substantial number of galaxies exhibiting mixed morphological structures due to their classification scheme with seven morphological types. Huertas-Company et al. (2023) and Tohill et al. (2023) also utilized more detailed subdivisions in their classification scheme than ours, employing CNN and unsupervised machine learning techniques. They found that irregular and clumpy galaxies become dominant beyond $z > 3$, with high fractions of disk-like morphologies in $\log M_*/M_\odot > 11$.

On the other hand, there have been several concerns about potential systematic uncertainties in morphology classification using JWST/NIRCam data. Vega-Ferrero et al. (2024) used a contrastive learning framework to investigate high-redshift galaxy morphology at $z \sim 3-6$ in CEERS, calibrating with mock data from the TNG50-1 simulation. Their results agreed with the disk dominance in the high-redshift universe, with approximately half of the galaxies classified as disks. However, they also noted that some compact and prolate-shaped galaxies might have been misclassified as pure disk galaxies, resulting in a potential overestimation of the disk fraction at $z > 3$. This is also supported by Pandya et al. (2024), which insisted that the Sérsic indices alone cannot distinguish prolate and oblate populations when considering the three-dimensional geometry of CEERS galaxies. Also using the CEERS field, Sun et al. (2024) analyzed the structures of 347 galaxies at $z = 4 - 9.5$, based on the two parameters of Sérsic indices and axis ratio. They carefully computed the uncertainties of the parameters, considering the influence of the pixel scale

when drizzling images, the PSF effects, and the cosmological effects depending on redshifts, such as surface brightness dimming, angular resolution, and sensitivity. Their robust tests showed that the redshift has little impact on the Sérsic index measurements up to at $z \lesssim 6$, but higher redshift could lead to underestimation of Sérsic indices for compact and spheroid-like ($n \gtrsim 2$) galaxies (see Figure B2 in their Appendix). Due to the systematic underestimation of the Sérsic indices, disk fraction at $z > 6$ could be overestimated by spheroid-like galaxies misclassified as disk-like galaxies. Despite these uncertainties, Sun et al. (2024) also agreed high incidence of disk galaxies at $z > 4$, providing the lower limit of disk fractions of $\sim 45\%$ with the parametric criteria of $n < 1.5$ and $b/a < 0.6$. We note that the systematic effect studied by Sun et al. (2024) would not significantly affect the morphological distributions of the JWST galaxies measured in this paper because only $\sim 20\%$ of our sample at $z = 4 - 8$ have redshift higher than 6 and almost 90% of the galaxies at $z > 6$ are not so compact, having Sérsic indices less than 1.7 (see the middle panel of Figure B2 in Sun et al. 2024).

In summary, previous JWST studies cannot be directly compared with one another as the classification criteria are all different. We adopt a simple but objective classification scheme that has been proven to be effective and can be directly compared to the HR5 cosmological simulation results. Although there are some differences and uncertainties in specific trends of morphological distributions, most JWST studies are in line with the disk dominance in the early universe.

6. SUMMARY

In this study, we examine the rest-frame optical morphologies of high-redshift galaxies using the JWST/NIRCam images obtained from six JWST fields: NEP-TDF, NGDEEP, CEERS, COSMOS, UDS, and SMACS0723. We select $\sim 19,000$ high-redshift galaxies with stellar masses of $\log M_*/M_\odot > 9$ and redshifts of $z = 0.6 - 8.0$, derived from the SED fitting procedure. We apply a parametric morphological classification scheme utilized in the HR5 simulation (Park et al. 2022) and compare our findings with the HR5 results. The key parameters for morphology classification (Sérsic index, asymmetry, and RFF) were derived from the JWST/NIRCam images through SExtractor photometry and a single Sérsic fitting with GALFIT. Following the methodology of the HR5 study, our classification scheme categorizes three morphological types: disks ($n < 1.5$, $A < 0.32$, and $RFF < 0.5$), spheroids ($n > 1.5$, $A < 0.32$, and $RFF < 0.5$), and irregulars

($A > 0.32$ or $RFF > 0.5$). From these analyses, our main results can be summarized as follows.

1. Our photometric redshift measurements from the SED fitting show an outlier fraction of $\sim 6\%$ with $\sigma_{\text{NMAD}} = 0.009$ for objects with $\chi_{\text{SED}}^2 < 20$ and $N_{\text{fit}} \geq 6$. This accuracy is superior to the previous studies using HST-only data, highlighting that JWST photometric data is beneficial to analyze the properties of a large sample of high-redshift galaxies. However, several outliers at $z_{\text{spec}} < 1$ exhibit overestimated photometric redshifts with $z_{\text{phot}} > 1$, potentially indicating low-redshift contaminants in our sample.
2. The distribution of asymmetry is strongly concentrated at $A = 0.2$ but skewed toward higher asymmetry values across all redshift ranges. This skewness occurs due to the existence of asymmetric galaxies with irregular substructures. The RFF values have positive correlations with asymmetry, with a median $RFF = 0.13$. The Sérsic indices tend to increase with stellar mass, implying that the formation of bulge-like structures is accompanied with mass growth of galaxies. The proportion of galaxies with bulge-like structures ($n > 1.5$) declines at $z > 3$ compared to the $z < 3$ universe. Potential biases of these parameters depending on the JWST fields have negligible effects on morphology classification.
3. Disk galaxies are dominant in the mass range of $\log M_*/M_\odot < 10.5$, with the disk fraction reaching up to $\sim 80\%$ at $z > 4$ in this mass range. However, the disk fraction decreases with increasing stellar mass across all redshift ranges. This implies that disks are likely to be the initial morphology of galaxies in the early universe and experience morphological transformations to spheroids or irregulars.
4. Spheroid galaxies are present at $z > 6$ with a fraction of $\lesssim 10\%$ of the galaxy population. However, the spheroid fraction increases as stellar mass increases and redshift decreases, becoming the dominant type in $\log M_*/M_\odot \gtrsim 10.5-11$ at $z < 3$. This spheroid dominance in the high-mass regime implies that the mass growth is associated with morphological transformation from disks to spheroids.
5. Irregular galaxies maintain a relatively constant fraction of $\sim 20\%$ with respect to stellar mass. In the morphological fraction as a function of redshift, however, the irregular fraction exhibits a

peak at $z \sim 2 - 3$ and decreases again below 20% in the $z < 1$ universe. This decrease in irregular fraction is mainly driven by a decrease in the number of massive irregulars ($\log M_*/M_\odot \gtrsim 10.5$), implying that irregular galaxies eventually transform into spheroid galaxies in the cosmic afternoon ($z < 1.5$).

6. The morphological distributions in the cosmic morning ($z > 4$) are consistent with the HR5 simulation, confirming the disk dominance in the early universe. As suggested in Park et al. (2022), disk galaxies in the cosmic morning evolve into spheroids and irregulars through merger and gas accretion. Massive irregular galaxies appear to be an intermediate phase in the morphological transition from disks to spheroids. These evolutionary tracks of galaxy morphology align well with the HR5 study, thus demonstrating that this study effectively verify the HR5 results with the JWST observational data.

The close agreement between our observational morphology distribution measurement and HR5 simulation results opens the possibility that the origin and evolution of galaxy morphology can be understood from cosmological simulations. It remains to be seen how future observational results with larger number of galaxies and improved redshift accuracy will compare with our measurement and also with the predictions of future cosmological simulations.

JHL was supported by the National Research Foundation of Korea (NRF) grant funded by the Korean government (MSIT) (Nos. 2022R1A4A3031306 and 2023R1A2C1006261). HSH acknowledges the support by the National Research Foundation of Korea (NRF) grant funded by the Korea government (MSIT) (No. 2021R1A2C1094577). This work is based on observations made with the NASA/ESA/CSA James Webb Space Telescope. The data were obtained from the Mikulski Archive for Space Telescopes (MAST) at the Space Telescope Science Institute (STScI), which is operated by the Association of Universities for Research in Astronomy, Inc., under NASA contract NAS 5-03127 for JWST. This research is based on observations made with the NASA/ESA Hubble Space Telescope obtained from STScI. Some/all of the data presented in this paper were obtained from the MAST at STScI. The specific observations analyzed can be accessed via <https://doi.org/10.17909/b7cb-xc61> (NEP-TDF), <https://doi.org/10.17909/hh6k-9z63> (NGDEEP), <https://doi.org/10.17909/fna5-we11> (CEERS), <https://doi.org/10.17909/tdx4-0a35> (COSMOS), <https://doi.org/10.17909/8kp6-9223> (UDS), and <https://doi.org/10.17909/8nfp-hr63> (SMACS0723).

Software: Astropy (Astropy Collaboration et al. 2013, 2018, 2022), EAZY-PY (Brammer et al. 2008; Brammer 2023b), GALFIT (Peng et al. 2002, 2010), Matplotlib (Hunter 2007), Numpy (Harris et al. 2020), PSFEX (Bertin 2011), Scipy (Virtanen et al. 2020), SOURCE EXTRACTOR (Bertin & Arnouts 1996), WEBBPSF (Perrin et al. 2014)

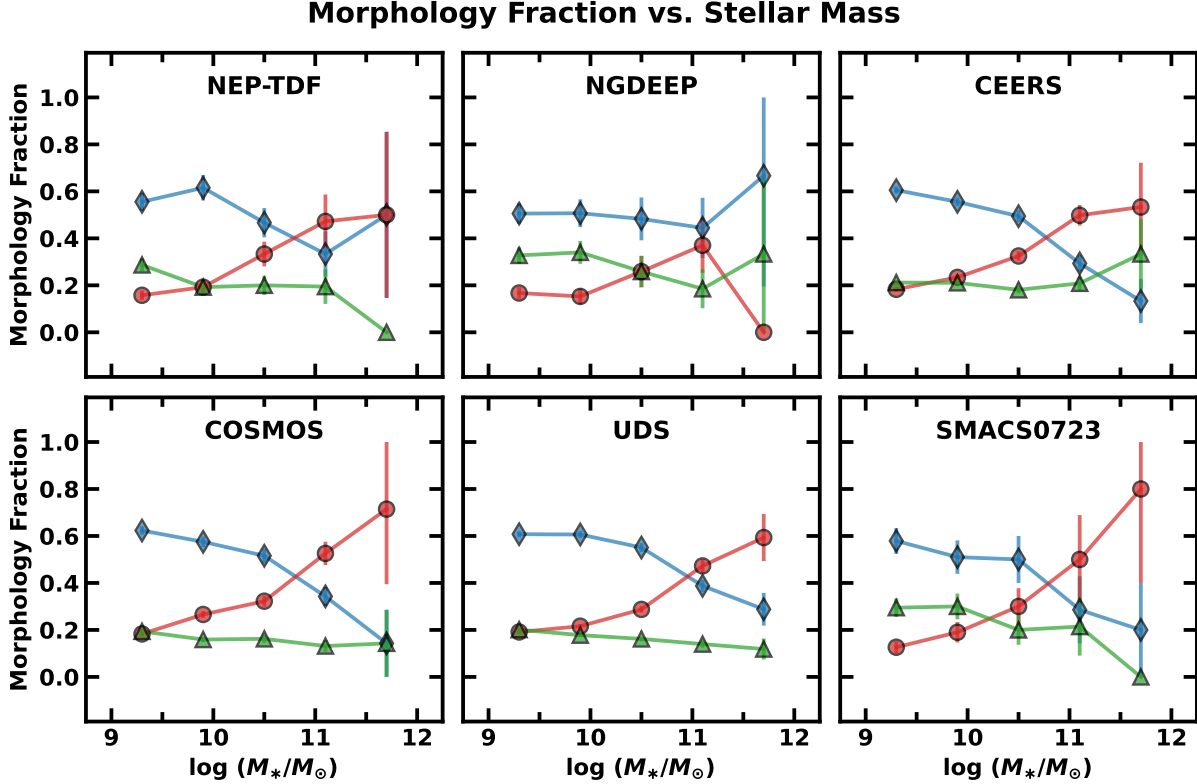


Figure A1. Same as the left panel of Figure 13, but for each JWST field.

APPENDIX

A. FIELD-TO-FIELD VARIATIONS IN MORPHOLOGICAL DISTRIBUTIONS

The use of six JWST fields with different depths can introduce variations in morphological distributions. As shown in Table 3, the outlier fraction of our photometric redshift measurements exhibits fluctuations across the JWST fields, indicating potential variances in the accuracy of stellar masses derived from the SED fitting. In addition, variations in background fluctuations can lead to systematic differences in the estimation of key parameters (n , A , and RFF) for morphology classification. To account for these variations, we measured the field-to-field deviations of morphological fractions in the mass and redshift bins, by calculating standard deviations of the fractions in each bin weighted by the number of samples in each field. The total uncertainties in Figures 12, 13, and 14 were determined by summing the squared field-to-field deviations and Poisson noises of the sample sizes in the bins. Here we illustrate the morphological fractions in the six JWST fields as functions of stellar mass and redshift in Figure A1 and Figure A2, respectively.

Figure A1 shows that disk galaxies have a dominant proportion of $\sim 60\%$ in $\log M_*/M_\odot < 10.5$ for all JWST fields. Although disk fractions generally decrease with increasing stellar mass, this trend is less discernible in the fields of NEP-TDF and NGDEEP due to their limited sample sizes in the mass bin of $\log M_*/M_\odot = 11.4 - 12.0$. Spheroidal fractions increase with stellar mass, but the data in the NGDEEP field suffer from the small number statistics in the highest mass bin. Irregular fractions remain constant at $\sim 20\%$, but show large fluctuations in the highest mass bin due to significant uncertainties. Irregular fractions in the NGDEEP field are higher than in other fields, due to relatively larger RFF values resulting from small background sigma values in Equation 2 (see Section 4.1). Although the data from the SMACS0723 field could be affected by gravitational lensing, the general tendency in this field is consistent with the stacked data in the left panel of Figure 13.

In Figure A2, disk galaxies also maintain dominance across all redshift ranges in all JWST fields. Decreases in disk fraction from $\sim 70\%$ at $z \gtrsim 3$ to $\sim 50\%$ at $z \lesssim 3$ are consistently observed in all fields. Despite fluctuations

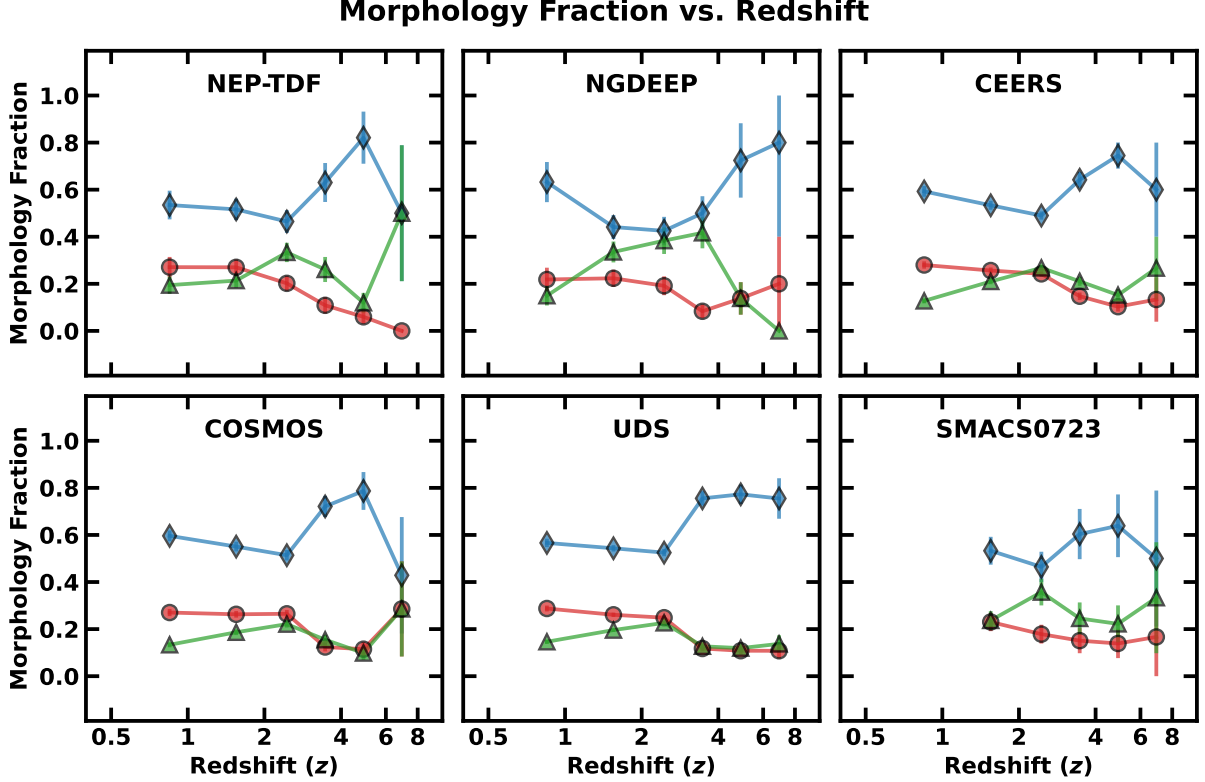


Figure A2. Same as the right panel of Figure 13, but for each JWST field.

in the disk fraction at the highest redshift bin ($z = 6.0 - 8.0$), the general trend appears unaffected by field-to-field variations. Spheroidal fractions consistently rise with decreasing redshift, except for the cases with only five spheroids in the high-redshift bins ($z = 4.0 - 8.0$) in the NGDEEP field. Irregular fractions also exhibit similar patterns across all JWST fields, peaking at over $\sim 25\%$ around $z \sim 2 - 3$. Like other morphological types, irregular fractions in the $z = 6.0 - 8.0$ bin are less reliable in the NEP-TDF and NGDEEP fields due to their small sample sizes (only 3 irregulars in the NEP-TDF and none in the NGDEEP). The NGDEEP field shows notably higher irregular fractions of about $\sim 40\%$ at $z = 2 - 3$ compared to other fields, for the reasons mentioned above.

These findings demonstrate that the general trends for each morphological type are not significantly affected by the field-to-field variations. However, these variations are still non-negligible, so we reflect these fluctuations across the JWST fields as the uncertainties of morphological fractions in the mass and redshift bins.

B. CONVERSION FROM THREE-DIMENSIONAL TO TWO-DIMENSIONAL ASYMMETRY

The asymmetry criterion of $A = 0.4$ applied in Park et al. (2022) to distinguish symmetric galaxies and asymmetric galaxies was established based on the three-dimensional distribution of stellar particles. Thus, the direct application of this criterion to the two-dimensional data of JWST images is not desirable. To address this, we conducted a simple test to determine a two-dimensional asymmetry criterion that corresponds to the three-dimensional asymmetry threshold of $A = 0.4$ employed based on the actual distribution A of the galaxies identified in HR5.

In Figure B1, we present a comparison between the three-dimensional asymmetry (A_{3D}) and the two-dimensional asymmetry (A_{2D}) of 2,669 simulated galaxies at $z \sim 6$ in the HR5 simulation. The two-dimensional asymmetry was measured using the same methodology described in Section 3.1 of Park et al. (2022), with the face-on projected stellar mass density profile. We searched for the optimal threshold value of $A_{2D} > X$ corresponding to $A_{3D} > 0.4$, which minimizes contamination and loss of completeness simultaneously.

Contamination quantifies the presence of contaminated sources within asymmetric objects selected with the $A_{2D} > X$ criterion, which was calculated as the number fraction of objects with $A_{2D} > X$ and $A_{3D} < 0.4$ relative to those with $A_{2D} > X$ and $A_{3D} > 0.4$. Completeness represents the fraction of objects with $A_{2D} > X$ and $A > 0.4$ relative to

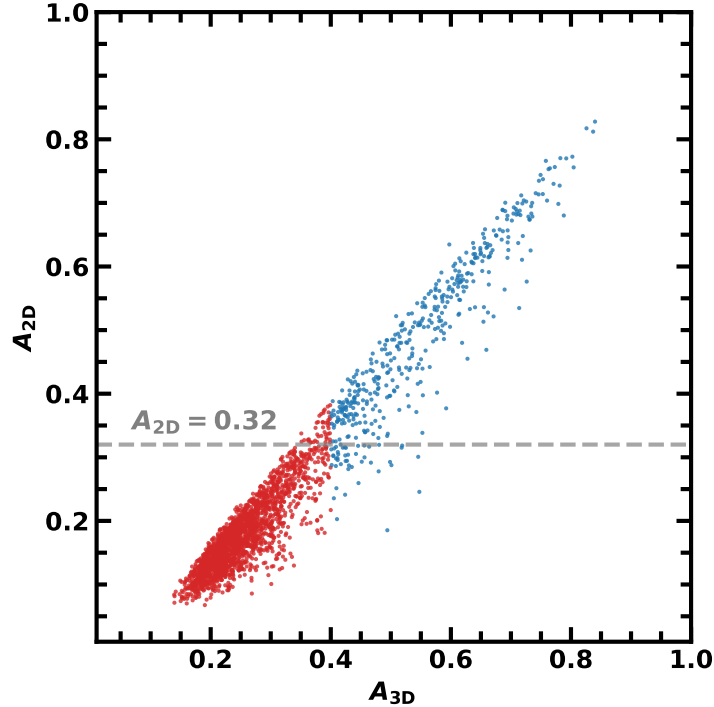


Figure B1. Comparison between the three-dimensional asymmetry (A_{3D} ; x-axis) and the two-dimensional asymmetry (A_{2D} ; y-axis). Blue circles denote the objects with $A_{3D} > 0.4$, which are defined as asymmetric galaxies in Park et al. (2022), while red circles represent the rests. Note that the division threshold of $A_{3D} = 0.4$ has been found based on the actual distribution A of the galaxies identified in HR5. Gray dashed line marks the asymmetry criterion of $A_{2D} = 0.32$ used in this study.

the total number of those with $A_{3D} > 0.4$, so loss of completeness is the opposite probability of the completeness. We determined the threshold for two-dimensional asymmetry at $X = 0.32$ (denoted by the black dashed line in the figure), yielding minimum values for both contamination and loss of completeness about $\sim 10\%$. This two-dimensional asymmetry criterion of $A_{2D} = 0.32$ was subsequently applied in our morphology classification, as detailed in Section 3.4.

C. UNCERTAINTIES OF MORPHOLOGICAL MEASUREMENTS FROM THE PSF MODELS

To test the effect of the PSF model for GALFIT, we generated new empirical PSFs with the pixel-based model using the PSFEX software, as done in Zhuang & Shen (2024). We set our configurations for selecting point sources, with the FWHM range (SAMPLE_FWHM_RANGE) of 1 – 4 pixels for short wavelength channels and 2 – 6 pixels for long wavelength channels, the minimum signal-to-noise ratio (SAMPLE_MINSN) of 100, and the maximum $(a - b)/(a + b)$ value (SAMPLE_MAXELLIP) of 0.15. The output PSF models are sampled with the pixel scale of $0''.04 \text{ pixel}^{-1}$, with the image size of $4'' \times 4''$. The PSF image size was set to be slightly smaller than that of WEBBPSF model ($5'' \times 5''$) due to possible light contamination from neighboring objects in real images. To account for spatial variations in PSFs, we manually divided the images of JWST fields into multiple regions, each of which encompasses the field of view of $\sim 2'.2 \times 2'.2$. From each region, we extracted the empirical PSF models from $\sim 5 - 15$ selected stars.

Figure C1 shows the radial light profiles of all PSF models. In all JWST/NIRCam bands, the empirical PSFs from PSFEX have broader profiles compared to the simulated PSF from WEBBPSF. This is also consistent with the profiles of empirical PSFs used in other JWST studies (Ono et al. 2023) because the drizzling effect of real NIRCam images can be reflected in empirical PSFs in contrast to simulated PSFs. Figure C2 shows the differences of Sérsic indices of our sample derived from PSFEX models and those from WEBBPSF. Across all NIRCam bands, the Sérsic index differences show considerable scatters about ~ 0.1 dex but little systematic biases. The Sérsic indices from the PSFEX models can be slightly increased in the high-mass regime compared to those from WEBBPSF because deconvolving galaxies with broader PSFs in GALFIT tend to result in more concentrated galaxy models with larger Sérsic indices. However, the median increases of the Sérsic indices are less than ~ 0.04 dex, leading to little systematic biases.

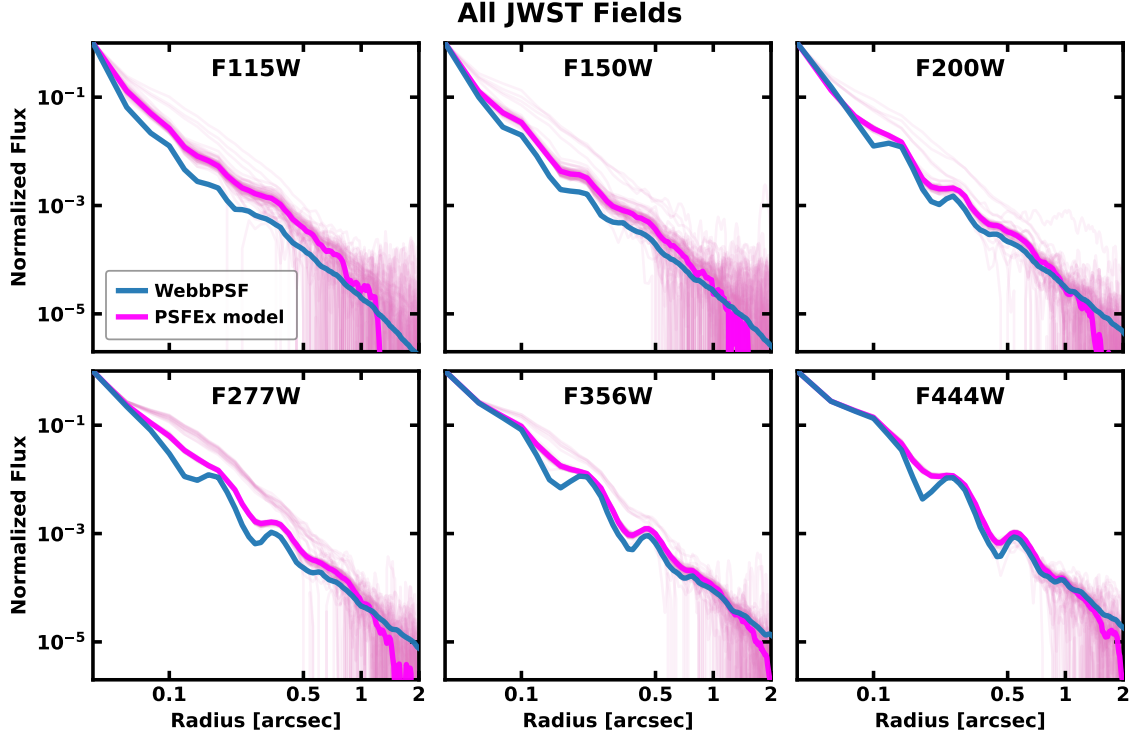


Figure C1. Radial profiles of PSF models for the six JWST/NIRCam bands. In a panel for each band, the blue thick lines represent the simulated PSF models generated by WEBBPSF, and the magenta thick lines represent the median profiles of empirical PSF models from PSFEX. The pale magenta lines show the profiles of all PSFEX models from each divided region, indicating the spatial variations of empirical PSFs.

Applying the PSFEX models, [Figure C3](#) shows the results of morphological fractions as a function of stellar mass. Comparing this figure to [Figure 12](#), the overall trends of morphological fractions do not change at all, still supporting our results. Thus, the choice of the PSF models does not have significant systematic effects on our main conclusions.

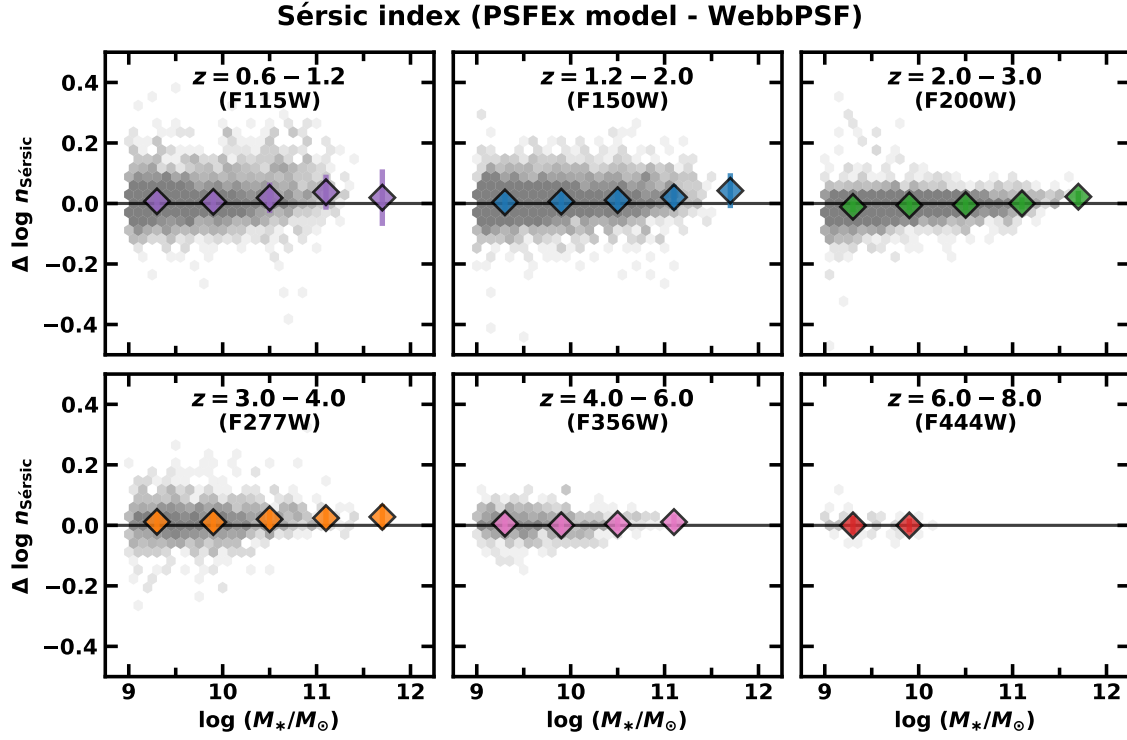


Figure C2. Same as Figure 11, but the y-axis value is the logarithmic differences between Sérsic indices derived from the empirical PSFs (PSFEx model) and those from the simulated PSFs (WEBBPSF).

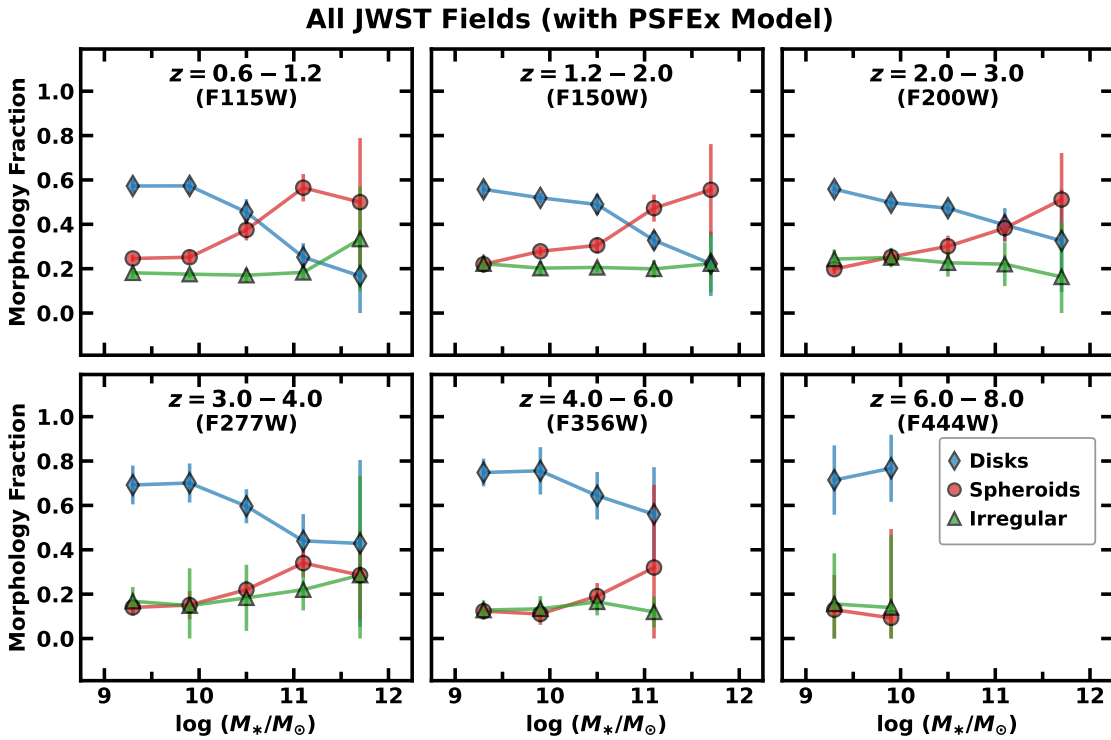


Figure C3. Same as Figure 12, but the results are derived from the empirical PSF models.

REFERENCES

- Abraham, R. G., van den Bergh, S., Glazebrook, K., et al. 1996, *ApJS*, 107, 1. doi:10.1086/192352
- Abraham, R. G. & van den Bergh, S. 2001, *Science*, 293, 1273. doi:10.1126/science.1060855
- Astropy Collaboration, Robitaille, T. P., Tollerud, E. J., et al. 2013, *A&A*, 558, A33. doi:10.1051/0004-6361/201322068
- Astropy Collaboration, Price-Whelan, A. M., Sipőcz, B. M., et al. 2018, *AJ*, 156, 123. doi:10.3847/1538-3881/aabc4f
- Astropy Collaboration, Price-Whelan, A. M., Lim, P. L., et al. 2022, *ApJ*, 935, 167. doi:10.3847/1538-4357/ac7c74
- Bagley, M. B., Pirzkal, N., Finkelstein, S. L., et al. 2023, arXiv:2302.05466. doi:10.48550/arXiv.2302.05466
- Bamford, S. P., Nichol, R. C., Baldry, I. K., et al. 2009, *MNRAS*, 393, 1324. doi:10.1111/j.1365-2966.2008.14252.x
- Barden, M., Häußler, B., Peng, C. Y., et al. 2012, *MNRAS*, 422, 449. doi:10.1111/j.1365-2966.2012.20619.x
- Benítez, N. 2000, *ApJ*, 536, 571. doi:10.1086/308947
- Bertin, E. & Arnouts, S. 1996, *A&AS*, 117, 393. doi:10.1051/aas:1996164
- Bertin, E. 2011, *Astronomical Data Analysis Software and Systems XX*, 442, 435
- Bezanson, R., Labbe, I., Whitaker, K. E., et al. 2022, arXiv:2212.04026. doi:10.48550/arXiv.2212.04026
- Bradley, L. D., Coe, D., Brammer, G., et al. 2023, *ApJ*, 955, 13. doi:10.3847/1538-4357/acecfe
- Brammer, G. B., van Dokkum, P. G., & Coppi, P. 2008, *ApJ*, 686, 1503. doi:10.1086/591786
- Brammer, Gabriel. (2023a). *grizli* (1.8). Zenodo. doi:10.5281/zenodo.7701739
- Brammer, Gabriel. (2023b). *eazy-py* (0.6.7). Zenodo. doi:10.5281/zenodo.8268031
- Buitrago, F., Trujillo, I., Conselice, C. J., et al. 2013, *MNRAS*, 428, 1460. doi:10.1093/mnras/sts124
- Calvi, R., Poggianti, B. M., Fasano, G., et al. 2012, *MNRAS*, 419, L14. doi:10.1111/j.1745-3933.2011.01168.x
- Cameron, E., Carollo, C. M., Oesch, P. A., et al. 2011, *ApJ*, 743, 146. doi:10.1088/0004-637X/743/2/146
- Carnall, A. C., Begley, R., McLeod, D. J., et al. 2023, *MNRAS*, 518, L45. doi:10.1093/mnras/slac136
- Casey, C. M., Kartaltepe, J. S., Drakos, N. E., et al. 2023, *ApJ*, 954, 31. doi:10.3847/1538-4357/acc2bc
- Coe, D., Salmon, B., Bradač, M., et al. 2019, *ApJ*, 884, 85. doi:10.3847/1538-4357/ab412b
- Conselice, C. J., Bershady, M. A., & Jangren, A. 2000, *ApJ*, 529, 886. doi:10.1086/308300
- Conselice, C. J. 2003, *ApJS*, 147, 1. doi:10.1086/375001
- Conselice, C. J., Blackburne, J. A., & Papovich, C. 2005, *ApJ*, 620, 564. doi:10.1086/426102
- Conselice, C. J., Rajgor, S., & Myers, R. 2008, *MNRAS*, 386, 909. doi:10.1111/j.1365-2966.2008.13069.x
- Dahlen, T., Mobasher, B., Dickinson, M., et al. 2007, *ApJ*, 654, 172. doi:10.1086/508854
- Dressler, A. 1980, *ApJ*, 236, 351. doi:10.1086/157753
- Duncan, K., Conselice, C. J., Mundy, C., et al. 2019, *ApJ*, 876, 110. doi:10.3847/1538-4357/ab148a
- Dunlop, J. S., Abraham, R. G., Ashby, M. L. N., et al. 2021, *JWST Proposal. Cycle 1*, 1837
- Fasano, G., Poggianti, B. M., Bettoni, D., et al. 2015, *MNRAS*, 449, 3927. doi:10.1093/mnras/stv500
- Ferreira, L., Adams, N., Conselice, C. J., et al. 2022, *ApJL*, 938, L2. doi:10.3847/2041-8213/ac947c
- Ferreira, L., Conselice, C. J., Sazonova, E., et al. 2023, *ApJ*, 955, 94. doi:10.3847/1538-4357/acec76
- Finkelstein, S. L., Dickinson, M., Ferguson, H. C., et al. 2017, *JWST Proposal ID 1345. Cycle 0 Early Release Science*, 1345
- Finkelstein, S. L., Papovich, C., Pirzkal, N., et al. 2021, *JWST Proposal. Cycle 1*, 2079
- Finkelstein, S. L., Bagley, M. B., Ferguson, H. C., et al. 2023, *ApJL*, 946, L13. doi:10.3847/2041-8213/acade4
- Gaia Collaboration, Brown, A. G. A., Vallenari, A., et al. 2021, *A&A*, 649, A1. doi:10.1051/0004-6361/202039657
- Galametz, A., Grazian, A., Fontana, A., et al. 2013, *ApJS*, 206, 10. doi:10.1088/0067-0049/206/2/10
- Green, G. M. 2018, *The Journal of Open Source Software*, 3, 695. doi:10.21105/joss.00695
- Harris, C. R., Millman, K. J., van der Walt, S. J., et al. 2020, *Nature*, 585, 357. doi:10.1038/s41586-020-2649-2
- Hoyos, C., den Brok, M., Verdoes Kleijn, G., et al. 2011, *MNRAS*, 411, 2439. doi:10.1111/j.1365-2966.2010.17855.x
- Hoyos, C., Aragón-Salamanca, A., Gray, M. E., et al. 2012, *MNRAS*, 419, 2703. doi:10.1111/j.1365-2966.2011.19918.x
- Hubble, E. P. 1926, *ApJ*, 64, 321. doi:10.1086/143018
- Huertas-Company, M., Tasca, L., Rouan, D., et al. 2009, *A&A*, 497, 743. doi:10.1051/0004-6361/200811255
- Huertas-Company, M., Bernardi, M., Pérez-González, P. G., et al. 2016, *MNRAS*, 462, 4495. doi:10.1093/mnras/stw1866
- Huertas-Company, M., Iyer, K. G., Angeloudi, E., et al. 2023, arXiv:2305.02478. doi:10.48550/arXiv.2305.02478
- Hunter, J. D. 2007, *Computing in Science and Engineering*, 9, 90. doi:10.1109/MCSE.2007.55
- Hwang, H. S. & Park, C. 2009, *ApJ*, 700, 791. doi:10.1088/0004-637X/700/1/791

- Ikeda, R., Morishita, T., Tsukui, T., et al. 2023, *MNRAS*, 523, 6310. doi:10.1093/mnras/stad1692
- Jacobs, C., Glazebrook, K., Calabrò, A., et al. 2023, *ApJL*, 948, L13. doi:10.3847/2041-8213/accd6d
- Kartaltepe, J., Casey, C. M., Bagley, M., et al. 2021, *JWST Proposal. Cycle 1*, 1727
- Kartaltepe, J. S., Rose, C., Vanderhoof, B. N., et al. 2023, *ApJL*, 946, L15. doi:10.3847/2041-8213/acad01
- Kron, R. G. 1980, *ApJS*, 43, 305. doi:10.1086/190669
- Lee, J., Shin, J., Snaith, O. N., et al. 2021, *ApJ*, 908, 11. doi:10.3847/1538-4357/abd08b
- Lotz, J. M., Primack, J., & Madau, P. 2004, *AJ*, 128, 163. doi:10.1086/421849
- Lotz, J. M., Madau, P., Giavalisco, M., et al. 2006, *ApJ*, 636, 592. doi:10.1086/497950
- Margalef-Bentabol, B., Conselice, C. J., Mortlock, A., et al. 2016, *MNRAS*, 461, 2728. doi:10.1093/mnras/stw1451
- Mortlock, A., Conselice, C. J., Hartley, W. G., et al. 2013, *MNRAS*, 433, 1185. doi:10.1093/mnras/stt793
- Nakajima, K., Ouchi, M., Isobe, Y., et al. 2023, *ApJS*, 269, 33. doi:10.3847/1538-4365/acd556
- Nelson, E. J., Suess, K. A., Bezanson, R., et al. 2023, *ApJL*, 948, L18. doi:10.3847/2041-8213/acc1e1
- Noirot, G., Desprez, G., Asada, Y., et al. 2023, *MNRAS*, 525, 1867. doi:10.1093/mnras/stad1019
- Ono, Y., Harikane, Y., Ouchi, M., et al. 2023, *ApJ*, 951, 72. doi:10.3847/1538-4357/acd44a
- Ormerod, K., Conselice, C. J., Adams, N. J., et al. 2023, *arXiv:2309.04377*. doi:10.48550/arXiv.2309.04377
- Pandya, V., Zhang, H., Huertas-Company, M., et al. 2024, *ApJ*, 963, 54. doi:10.3847/1538-4357/ad1a13
- Papovich, C., Dickinson, M., Giavalisco, M., et al. 2005, *ApJ*, 631, 101. doi:10.1086/429120
- Park, C. & Choi, Y.-Y. 2005, *ApJL*, 635, L29. doi:10.1086/499243
- Park, C., Choi, Y.-Y., Vogeley, M. S., Gott, J. R., & Blanton, M. R. 2007, *ApJ*, 658, 898.
- Park, C., Gott, J. R., & Choi, Y.-Y. 2008, *ApJ*, 674, 784. doi:10.1086/524192
- Park, C. & Choi, Y.-Y. 2009, *ApJ*, 691, 1828. doi:10.1088/0004-637X/691/2/1828
- Park, C. & Hwang, H. S. 2009, *ApJ*, 699, 1595. doi:10.1088/0004-637X/699/2/1595
- Park, C., Lee, J., Kim, J., et al. 2022, *ApJ*, 937, 15. doi:10.3847/1538-4357/ac85b5
- Peebles, P. J. E. 1969, *ApJ*, 155, 393. doi:10.1086/149876
- Peng, C. Y., Ho, L. C., Impey, C. D., et al. 2002, *AJ*, 124, 266. doi:10.1086/340952
- Peng, C. Y., Ho, L. C., Impey, C. D., et al. 2010, *AJ*, 139, 2097. doi:10.1088/0004-6256/139/6/2097
- Perrin, M. D., Sivaramakrishnan, A., Lajoie, C.-P., et al. 2014, *Proc. SPIE*, 9143, 91433X. doi:10.1117/12.2056689
- Petrosian, V. 1976, *ApJL*, 210, L53. doi:10.1086/182301
- Planck Collaboration, Ade, P. A. R., Aghanim, N., et al. 2016, *A&A*, 594, A13. doi:10.1051/0004-6361/201525830
- Pontoppidan, K. M., Barrientes, J., Blome, C., et al. 2022, *ApJL*, 936, L14. doi:10.3847/2041-8213/ac8a4e
- Postman, M., Franx, M., Cross, N. J. G., et al. 2005, *ApJ*, 623, 721. doi:10.1086/428881
- Rigby, J., Perrin, M., McElwain, M., et al. 2023, *PASP*, 135, 048001. doi:10.1088/1538-3873/acb293
- Robertson, B. E., Tacchella, S., Johnson, B. D., et al. 2023, *ApJL*, 942, L42. doi:10.3847/2041-8213/aca086
- Sandage, A. 1961, Washington: Carnegie Institution, 1961
- Schlawin, E., Leisenring, J., Misselt, K., et al. 2020, *AJ*, 160, 231. doi:10.3847/1538-3881/abb811
- Schlegel, D. J., Finkbeiner, D. P., & Davis, M. 1998, *ApJ*, 500, 525. doi:10.1086/305772
- Sun, W., Ho, L. C., Zhuang, M.-Y., et al. 2024, *ApJ*, 960, 104. doi:10.3847/1538-4357/acf1f6
- Tohill, C.-B., Bamford, S., Conselice, C., et al. 2023, *arXiv:2306.17225*. doi:10.48550/arXiv.2306.17225
- Valentino, F., Brammer, G., Gould, K. M. L., et al. 2023, *ApJ*, 947, 20. doi:10.3847/1538-4357/acbefa
- Vega-Ferrero, J., Huertas-Company, M., Costantin, L., et al. 2024, *ApJ*, 961, 51. doi:10.3847/1538-4357/ad05bb
- Virtanen, P., Gommers, R., Oliphant, T. E., et al. 2020, *Nature Methods*, 17, 261. doi:10.1038/s41592-019-0686-2
- Vulcani, B., Poggianti, B. M., Aragón-Salamanca, A., et al. 2011, *MNRAS*, 412, 246. doi:10.1111/j.1365-2966.2010.17904.x
- Ward, E. M., de la Vega, A., Mobasher, B., et al. 2023, *arXiv:2311.02162*. doi:10.48550/arXiv.2311.02162
- Weaver, J. R., Cutler, S. E., Pan, R., et al. 2023, *arXiv:2301.02671*. doi:10.48550/arXiv.2301.02671
- Welker, C., Devriendt, J., Dubois, Y., et al. 2014, *MNRAS*, 445, L46. doi:10.1093/mnrasl/slu106
- White, S. D. M. 1984, *ApJ*, 286, 38. doi:10.1086/162573
- Windhorst, R. A., Ashcraft, T. A., Broadhurst, T. J., et al. 2022, *JWST Proposal. Cycle 1*, 2738
- Windhorst, R. A., Cohen, S. H., Jansen, R. A., et al. 2023, *AJ*, 165, 13. doi:10.3847/1538-3881/aca163
- Zhuang, M.-Y. & Shen, Y. 2024, *ApJ*, 962, 139. doi:10.3847/1538-4357/ad1183